2018

Free Swimming Bio-Inspired Hydrofoils in Unsteady Ground Effect

Jackson Heath Cochran-Carney
Lehigh University, jhcc2013@gmail.com

Free Swimming Bio-Inspired Hydrofoils in Unsteady Ground Effect

By

Jackson H. Cochran-Carney

A Thesis

Presented to the Graduate and Research Committee

of Lehigh University

in Candidacy for the Degree of

Master of Science

in

Mechanical Engineering

Lehigh University

August 2018

This thesis is accepted and approved in partial fulfillment of the requirements for the Master of Science.

_____

Date

_____

Dr. Keith W. Moored, Thesis Advisor

_____

Dr. D. Gary Harlow, Department Chair

Department of Mechanical Engineering and Mechanics

Acknowledgments

There are a number of people I would like to thank and attribute the success of this thesis work to. First and foremost, I'd like to thank my thesis advisor, Dr. Keith Moored. His guidance and support throughout my time in graduate school was appreciated immensely. His contributions to what I've learned in both the academic and professional realms are immeasurable.

I would also like to thank my lab mates for their support and insights throughout the duration of my work. Issues with debugging code or interpreting equations was always met with a genuine willingness to help and explain. This work would have struggled to materialize without them.

Finally, I would like to thank my family and friends for their constant support and motivation. To my parents and brother, Cynthia, Jeffrey, and Joshua, thank you for your unending positivity and encouragement during even the most demanding of times. To my best friends, Ally Fraser and Michael Song, thank you for the constant source of laughs and coffee breaks. This work would not have been possible without all of you.

Contents

Acknowledgments **iv**

List of Tables **vii**

List of Figures **viii**

Nomenclature and Symbols **xv**

Abstract **1**

1 Introduction **2**

1.1 Motivation 2

1.2 Background 3

1.3 Literature Review 4

2 Problem Description and Solving Methodology **7**

2.1 Problem Formulation 7

2.2 Governing Equations 14

2.3 Derivation of Boundary Integral Equation 17

2.4 Boundary Conditions and their Application 19

2.5 Numerical Solution to the Boundary Integral Equation 20
2.6 Wake Model 26
2.7 Solution Convergence 30
2.8 Validation 30
2.9 Implementation of the Solid Boundary 34
2.10 Free Swimming Implementation 35

3 Results **37**
3.1 Single Translational Degree of Freedom 37
3.2 Multiple Translational Degrees of Freedom 53

4 Conclusion **64**
4.1 Future Work 65

Bibliography **66**

Vita **70**

List of Tables

2.1 Parameter space for single degree-of-freedom simulations. . . . 13

2.2 Parameter space for multi degree-of-freedom simulations. . . . 13

List of Figures

2.1 (a) Schematic of virtual body, propulsor, and wake elements in the computational domain. (b) Side profile view of a generic fish with the differences between wetted surface area and propulsor planform area ideantified. 8

2.2 Streamlines of source and doublet panels. 21

2.3 NACA 0012 airfoil with a singularity body panel configuration following a cosine distribution. The concentration of body panels is larger at the leading and trailing edges to ensure reasonable surface resolution. 22

2.4 Panel based coordinate system that results from rotation matrix applied to global coordinate system. 23

2.5 At each time step a wake element is shed from the propulsor's trailing edge into the computational domain. Each scatter point corresponds to a doublet wake panel's endpoint. The wake elements are colored to reflect its strength and rotation. 29

2.6 Convergence of trajectory with increasing spacial and temporal resolution. 31

2.7 Comparison of potential flow solver solution with analytical solution. Solid line (-) corresponds to the analytical solution and scatter points (o) correspond to the potential flow solver solution. t/T is normalized time. 33

2.8 A zero flux ground plane is created via the method images. (a) Two propulsor's are placed within the computational domain with out-of-phase pitching kinematics to create a symmetry plane at $z = 0$. This automatically satisfies the no-flux boundary condition. (b) The resulting equivalent representation of the multi-body problem is akin to a single propulsor swimming near a solid boundary. 35

3.1 Trajectory data for hydrofoils with with $St = 0.2$, $k = 0.5$, $m^* = 10$, $D_0^* = 0.75$ for different initial pitching conditions. (a) Instantaneous leading-edge position (b) Cycle-averaged leading edge position. The dark and light lines correspond to a pitch-up and pitch-down condition, respectively. 38

3.2 Trajectory data for hydrofoils with $St = 0.2$, $k = 0.5$, and $m^* = 10$ for different initial pitching conditions and lateral starting positions. (a) Instantaneous leading-edge position. (b) Cycle-averaged leading edge position. The dark and light lines correspond to a pitch-up and pitch-down condition, respectively. 39

3.3 Unstable trajectory data for hydrofoils with $St = 0.2$, $k = 1.0$, $m^* = 3$, and $D_0^* = 0.25$ for different initial pitching conditions. (a) Instantaneous leading-edge position. (b) Cycle-averaged leading edge position. The dark and light lines correspond to a pitch-up and pitch-down condition, respectively. 40

3.4 Wake structures corresponding to steady-state hydrofoils undergoing varying initial pitching conditions at all D_0^* values considered. 41

3.5 Trajectory data for hydrofoils with $St = 0.2$, $k = 0.5$, and $D_0^* = 0.25$ for different non-dimensional masses. (a) Instantaneous leading-edge position. (b) Cycle-averaged leading edge position. The line colors, from darkest to lightest, correspond to $m^* = 3, 10, 20$. 41

3.6 Trajectory data for hydrofoils with $St = 0.35$, $k = 1$, and $D_0^* = 0.50$ for different non-dimensional masses. (a) Instantaneous leading-edge position. (b) Cycle-averaged leading edge position. The line colors, from darkest to lightest, correspond to $m^* = 3, 10, 20$. 42

3.7 Wake structures corresponding to steady-state hydrofoils with varying non-dimensional masses for $St = 0.20, 0.35$. 43

3.8 Cycle-averaged propuslive efficiency data for a hydrofoil with $St = 0.2$, $k = 0.5$, and $D_0^* = 0.25$ for varying m^* values. The line colors, from darkest to lightest, correspond to $m^* = 3, 10, 20$. The dashed line corresponds to a propulsor with infinite mass operating out of ground effect. 44

3.9 Cycle-averaged non-dimensional thrust data for a hydrofoil with $St = 0.2$, $k = 0.5$, and $D_0^* = 0.25$ for varying m^* values. The line colors, from darkest to lightest, correspond to $m^* = 3, 10, 20$. The dashed line corresponds to a propulsor with infinite mass operating out of ground effect. 45

3.10 Trajectory data for hydrofoils with $k = 1.0$, $D_0^* = 0.25$, and $m^* = 3.0$ for different St values. (a) Instantaneous leading-edge position. (b) Cycle-averaged leading edge position. The line colors, from darkest to lightest, correspond to $St = 0.2, 0.35, 0.5$. 46

3.11 Cycle-averaged propulsive efficiency data for a hydrofoil with $k = 1.0$, $D_0^* = 0.25$, and $m^* = 3$ for all St values considered. The line colors, from darkest to lightest, correspond to $St = 0.2, 0.35, 0.5$. 47

3.12 Cycle-averaged non-dimensional thrust data for a hydrofoil with $k = 1.0$, $D_0^* = 0.25$, and $m^* = 3$ for all St values considered. The line colors, from darkest to lightest, correspond to $St = 0.2, 0.35, 0.5$. 48

3.13 Wake structures corresponding to steady-state hydrofoils with $m^* = 3$, $D_0^* = 0.25$, $k = 1.0$ for various St values. 49

3.14 Trajectory data for hydrofoils with $D_0^* = 0.75$, $St = 0.2$, and $m^* = 10$ for different k values. (a) Instantaneous leading-edge position. (b) Cycle-averaged leading edge position. The line colors, from darkest to lightest, correspond to $k = 0.5, 1.0$. . . 49

3.15 Cycle-averaged propulsive efficiency data for a hydrofoil with $D_0^* = 0.75$, $St = 0.2$, and $m^* = 10$ for different k values. The line colors, from darkest to lightest, correspond to $k = 0.5, 1.0$. 50

3.16 Cycle-averaged non-dimensional thrust data for a hydrofoil with $D_0^* = 0.75$, $St = 0.2$, and $m^* = 10$ for all k values considered. The line colors, from darkest to lightest, correspond to $k = \pi/2, \pi$. 51

3.17 Wake structures corresponding to steady-state hydrofoils with $D_0^* = 0.75$, $St = 0.2$, and $m^* = 10$ for various k values. 52

3.18 Trajectory data for hydrofoils with $D_0^* = 0.25$, $A^* = 0.25$, and $m^* = 10$ for different initial pitch directions. (a) Instantaneous leading-edge position. (b) Cycle-averaged leading edge position. The line colors, from darkest to lightest, correspond to $\phi = 0°, 180°$. 54

3.19 Trajectory data for hydrofoils with $A^* = 0.25$ and $m^* = 10$ for all D_0^* values considered. (a) Instantaneous leading-edge position. (b) Cycle-averaged leading edge position. The line colors, from darkest to lightest, correspond to $D_0^* = 0.25, 0.50, 0.75$ 55

3.20 Wake structures corresponding to steady-state hydrofoils with $A^* = 0.25$ and $m^* = 10$ for various initial pitching (ϕ) conditions. 55

3.21 Trajectory data for hydrofoils with $A^* = 0.25$ and $D_0^* = 0.25$ for all m^* values considered. (a) Instantaneous leading-edge position. (b) Cycle-averaged leading edge position. The line colors, from darkest to lightest, correspond to $m^* = 3, 10, 20$. 56

3.22 Cycle-averaged propulsive efficiency data for a hydrofoil with $A^* = 0.25$ and $D_0^* = 0.25$ for all m^* values considered. The line colors, from darkest to lightest, correspond to $m^* = 3, 10, 20$. . 57

3.23 Swimming speed data for a hydrofoil with $A^* = 0.25$ and $D_0^* = 0.25$ for all m^* values considered. (a) Instantaneous freestream velocity. (b) Cycle-averaged freestream velocity. The line colors, from darkest to lightest, correspond to $m^* = 3, 10, 20$. . . 58

3.24 Wake structures corresponding to steady-state hydrofoils with $A^* = 0.25$ and $D_0^* = 0.25$ for various m^* values. 59

3.25 Trajectory data for hydrofoils with $D_0^* = 0.25$ and $m^* = 3$ for all A^* values considered. (a) Instantaneous leading-edge position. (b) Cycle-averaged leading edge position. The line colors, from darkest to lightest, correspond to $A^* = 0.25, 0.5, 0.75$. 60

3.26 Cycle-averaged propulsive efficiency data for a hydrofoil with $D_0^* = 0.25$ and $m^* = 3$ for all A^* values considered. The line colors, from darkest to lightest, correspond to $A^* = 0.25, 0.5, 0.75$. 61

3.27 Swimming speed data for a hydrofoil with $D_0^* = 0.25$ and $m^* = 3$ for all A^* values considered. (a) Instantaneous freestream velocity. (b) Cycle-averaged freestream velocity. The line colors, from darkest to lightest, correspond to $A^* = 0.25, 0.5, 0.75$. . . 61

3.28 Wake structures corresponding to steady-state hydrofoils with $D_0^* = 0.25$ and $m^* = 3$ for various A^* values. 63

Nomenclature and Symbols

Φ	Perturbation Potential	$\boldsymbol{u}$	Velocity Vector Field
(X, Z)	Inertial Coordinate System	(x, z)	Lagrangian Coordinate System
U	Swimming Speed	W	Cross-stream Body Velocity
P	Pressure	ρ	Fluid Density
$\mathcal{S}_b$	Propulsor Surface	$\mathcal{S}_w$	Wake Surface
L	Lift	T	Thrust
D	Drag	P	Power
C_L	Coefficient of Lift	C_T	Coefficient of Thrust
C_P	Coefficient of Power	C_D	Coefficient of Drag
$G(\boldsymbol{r}; \boldsymbol{r_0})$	Green's Function	σ	Source Strength
μ	Doublet Strength	L_{TE}	Trailing Edge Length
Δt	Time step	f	Frequency
A	Pitching Amplitude	ϕ	Pitching Phase Delay
Γ	Circulation	δ	Vortex Desingularization Parameter
c	Chord Length	St	Strouhal Number
k	Reduced Frequency	$C(k)$	Lift Deficiency Function
Re	Reynold's Number	S_w	Wetted Surface Area
S_p	Propulsar Surface Area	s	Span
d	Leading Edge Ground Distance	D^*	Non-dimensional Ground Distance
Li	Lighthill Number	η	Propulsive Efficiency

Abstract

A free-swimming potential flow analysis of unsteady ground effect is conducted for self-propelled, two-dimensional hydrofoils via a method of images. The foils undergo a pure pitching motion about their leading edge, and the positions of the body in the stream-wise and cross-stream directions are determined by the equations of motion of the body. It is shown that the unconstrained swimmer is attracted to a time-averaged position that is mediated by the flow interaction with the ground. The robustness of this fluid-mediated equilibrium position is probed by varying the non-dimensional mass, initial conditions and kinematic parameters of motion. Comparisons to the foils fixed-motion counterpart are also made to pinpoint the effect that free swimming near the ground has on wake structures and the fluid-mediated forces over time. Optimal swimming regimes for near-boundary swimming are then determined and elaborated upon.

Chapter 1

Introduction

1.1 Motivation

The idea of utilizing nature and biological systems as inspiration for design (biomimetics) has a rich and fascinating history. From utilizing flexible, insect-like blades for more efficient wind turbines [1] to reducing flight noise using an owl-inspired wing surface [2], many realms of science have benefited from the perfected performance mechanisms different species have developed through billions of years of trial-and-error. Within the realm of bio-propulsion, it has been observed that different species of fish propel themselves utilizing periodic pitching, flapping, and undulatory body motions [3]. This type of locomotion has been studied both experimentally [4] and numerically [5, 6] to find considerable efficiency advantages compared to other locomotion techniques [7]. Studies have further suggested substrate swimmers may harness additional hydrodynamic advantages due to their proximity to the ground. This thesis aims

to probe this hypothesis and provide a potential explanation for this behavior by quantifying performance metrics for unsteady, near-ground swimmers.

1.2 Background

Ground effect is an aerodynamic phenomenon that occurs when lifting surfaces (airfoils, hydrofoils, etc.) operate near a solid boundary (traditionally the ground), achieving higher lift-to-drag ratios. Steady ground effect has been studied extensively for fixed wing aircraft undergoing steady flight [8]. However, our knowledge of ground effect decreases substantially for non-fixed surfaces in unsteady flows. It is proposed that there are similar benefits to be gained by operating near a solid boundary in an unsteady fashion. The use of unsteady ground effect may have manifested in biological systems due to these proposed benefits and can be observed in species of birds, fish, and insects that propel themselves near a solid boundary [9, 10, 11]. For example, steelhead trout have been found to reduce their consumption of energy while swimming near the walls of a channel [12]. With a greater understanding of unsteady ground effect and its benefits, one may quantify the performance of biological systems more accurately and design effective unsteady propulsors for applications in Autonomous Underwater Vehicles (AUVs).

This thesis presents the foundation for an unsteady potential flow framework to model hydrofoils and biological propulsors in unsteady ground effect in order to discover and quantify any theorized benefits. Within this framework, a "free-swimming" module is incorporated to expand upon the findings of pre-

vious ground effect studies [8]. The coupling allows the simulated propulsor to freely translate in the streamwise and/or cross-stream directions and results in a more accurate representation of a biological swimmer, laying the groundwork for other degrees of freedom to be incorporated.

1.3 Literature Review

The bio-inspired unsteady ground effect problem is a relatively new research endeavor with a relatively small amount of available literature. The problem has been studied via asymptotic methods to predict lift and drag forces on oscillating wings [13]. In this work, however, only the case of "weak" ground effect was considered where the propulsor's distance from the ground is much greater than its characteristic length. The much more interesting case of moderate to extreme unsteady ground effect, where the propulsor's distance to the ground is less than the propulsor's characteristic length, was not analyzed. Unsteady ground effect has also been studied analytically by applying the linearized Euler equations to a flexible flat plate in channel flow [14]. However, the channel flow implementation resulted in solid boundaries above and below the plate which is not representative of conventional ground effect.

Although several studies have researched the unsteady ground effect problem numerically [15, 16], a majority of these studies only considered the hovering problem and neglected streamwise (thrust and drag) forces. The few studies to include these effects utilized inverted Formula One car front wings undergoing pure heave oscillations [17, 18]. Despite these propulsors having no

biological significance, the studies operated in a flow regime where streamwise forces were dominated by viscous effects. These results were unable to conclude if benefits exhibited by unsteady ground effect are a function of viscous considerations. Previous inviscid investigations have found that flexible, heaving plates in ground effect exhibit hydrodynamic benefits [19]. However we wish to discern whether these benefits extend to rigid, self-propelled swimmers.

The literature available for the experimental study of unsteady ground effect is even more limited. A pitching and heaving flexible fin modeled after a freshwater stingray was found to have no substantial benefits due to near-ground swimming [20]. It is difficult to attribute these findings to any one mechanism, as the fin was three-dimensional, flexible, and utilized a combination of propulsion kinematics. This thesis aims to isolate the benefits presented by unsteady ground effect by considering a simpler propulsor with less potential variables to attribute various propulsive benefits (or lack thereof). It has also been found that hydrodynamic benefits occur for pure pitching hydrofoils at stable equilibrium positions that vary as a function of Strouhal number [21]. This finding, however, did not consider self-propelled hydrofoils.

We believe we may fill a gap present in the current unsteady ground effect literature by coupling an unsteady potential flow solver with kinematic equations of motion to produce a free-swimmer. Additional kinematic degrees-of-freedom beg the following questions: are the propulsors attracted to a time-averaged equilibrium position with the implementation of self-propulsion in the freestream and cross-stream directions, does the propulsor observe any hydrodynamic benefits at these equilibrium positions, and how does the wake

structure behind the propulsor evolve as it moves towards and finds an equilibrium position?

Chapter 2

Problem Description and Solving Methodology

2.1 Problem Formulation

The performance of bio-inspired propulsors swimming near a solid boundary is quantified by performing a computational study on an idealized swimmer. The swimmer's performance metrics are studied under two distinct swimming conditions: unconstrained dynamics in the cross-stream direction (fixed swimming speed) and unconstrained dynamics in both the cross-stream and freestream directions (variable swimming speed). In the latter case, the swimmer is assumed to be self-propelled, made up of a virtual body and a two-dimensional hydrofoil pitching about its leading edge. Although the virtual body is not physically modeled within the computational domain, its presence is acknowledged by the application of a drag force, D. This drag force resists the motion

of the swimmer as it propels itself through the fluid medium. The magnitude of this opposing force is calculated following a form drag law appropriate for high Reynold's number flows ($Re = \mathcal{O}(10^4)$) [22]:

$$D = \frac{1}{2}\rho C_D S_w U^2 \tag{2.1}$$

where ρ is the fluid density, C_D is the coefficient of drag, S_w is the wetted surface area of the hydrofoil, and U is the hydrofoil's free-stream propulsion speed. A single C_D value of 0.03 is utilized in this study to aid in restricting the growth of the parameter space. This drag coefficient is a good average parameter that is representative of many swimming biological species [23, 24, 25, 26, 27, 28, 29].

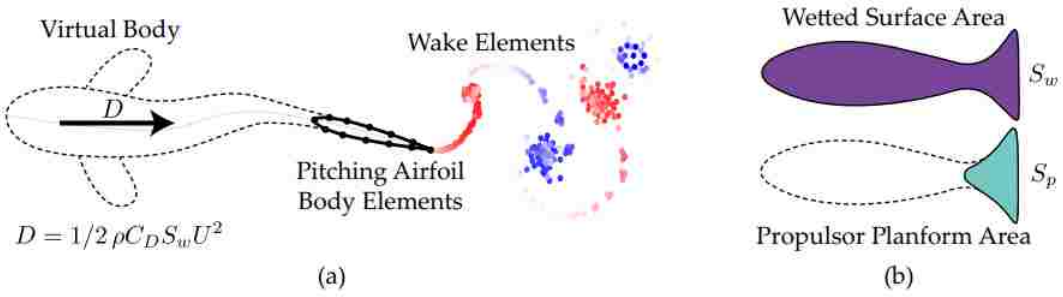

Figure 2.1: (a) Schematic of virtual body, propulsor, and wake elements in the computational domain. (b) Side profile view of a generic fish with the differences between wetted surface area and propulsor planform area ideantified.

We now define a ratio between the surface area exposed to the fluid, S_w, and the surface area of the propulsor, S_p:

$$S_{wp} \equiv \frac{S_w}{S_p} \tag{2.2}$$

The current study utilizes a single value of $S_{wp} = 10$ to further restrict the parameter space and allow for the analysis of variables that dictate kinematic motion. It is assumed the planform area is rectangular in shape and thus can be calculated simply by:

$$S_p = sc \tag{2.3}$$

where s is the propulsor's span and c is the propulsor's chord length. The propulsor's span is set to unity due to the two-dimensional nature of the problem. The S_{wp} and S_p parameters may be varied considerably in future works to study the effects of varying planform area to more closely model other species of ground swimmers.

An important non-dimensional term that hinges upon the wetted-planform area ratio and drag characteristics of a swimmer is the Lighthill number [30, 31]:

$$Li \equiv S_{wp} C_D \tag{2.4}$$

This number characterizes the thrust-drag trade off encountered by a self-propelled swimmer due to body and propulsor shape. For example, a large Lighthill number translates to a swimmer that produces a large amount of drag at low swimming speeds. This manifests as a low self-propelled swimming speed. The fixed values of S_{wp} and C_D result in a single Li value of 0.3, a reasonable number for several biological species [31]. It is important to note that prescribing Li will only have an effect on the multiple degree-of-freedom free-swimming analysis, as drag is only considered for self-propulsion.

We follow [8] and [32] by utilizing a 10% thick teardrop hydrofoil to model

the propulsor. Several non-dimensional mass terms are prescribed to study the effect of body mass on performance.The non-dimensional mass results from normalizing the body mass with the added-mass of the propulsor:

$$m^* \equiv \frac{m}{\rho S_p c} \tag{2.5}$$

The first non-dimensional mass value is chosen following [33] for its biological significance. Latter values are increased substantially to approach the static, non-free swimming cases presented in [21].

The prescribed kinematic motion of the foil is restricted to pure pitching about its leading edge. This pitching behavior is dictated by a pitching frequency, f, a peak-to-peak pitching amplitude, A, and a pitching phase delay, ϕ. The pitching amplitude is non-dimensionalized by the chord length:

$$A^* = \frac{A}{c} \tag{2.6}$$

This amplitude-to-chord ratio now defines the maximum pitching angle of the foil as:

$$\theta_0 = \sin^{-1}(\frac{A^*}{2}) \tag{2.7}$$

The instantaneous pitching angle of the hydrofoil, θ, is consequently defined by:

$$\theta(t) = \theta_0 \sin(2\pi f t + \phi) \tag{2.8}$$

The pitch phase delay term, ϕ, is set to either 0° or 180° to observe the effect of pitch direction on the steady-state solution. The hydrofoil will always begin

at a zero pitch angle but will vary in the direction it initially pitches.

The distance between the leading edge of the hydrofoil and the solid boundary, d, is non-dimensionalized by the chord length:

$$D^* = \frac{d}{c} \tag{2.9}$$

The lateral position of the propulsor's leading edge at the beginning of a simulation is denoted by D_0^*. We wish to study how the starting location of the propulsor effects the steady-state equilibrium position, wake structure, and performance metrics. Three initial propulsor locations of $D_0^* = 0.25, 0.50, 0.75$ are prescribed following the results presented in [8]. It is expected that these initial positions will uncover the different equilibrium attraction modes of increase, maintain, and decrease mean ground distance.

We now define additional non-dimensional terms that will aid in mapping out the desired parameter space. The reduced frequency, k, is defined as:

$$k \equiv \frac{fc}{U} \tag{2.10}$$

The reduced frequency conveys the degree of unsteadiness of the flow. More specifically, it represents the time it takes a fluid particle to travel a single chord length of the propulsor compared to one period of pitching oscillation. Large reduced frequencies correspond to highly unsteady flows where forces are dominated by added-mass effects. Conversely, small reduced frequencies represent quasi-static flows where forces are circulatory driven. Three reduced frequency values of $k = 0.5, 1.0, 2.0$ are analyzed following the results presented

in previous unsteady ground effect studies [8].

An additional non-dimensional term is the Strouhal number:

$$St \equiv \frac{fA}{U} \tag{2.11}$$

The Strouhal number can be interpreted as the distance ratio of adjacent wake vortices in the cross-stream and streamwise directions. When the amplitude of motion is held constant, a larger Strouhal number will result in wake vortices that are closer together in the streamwise direction. This closer "packing" of vortices results in more pronounced wake influence on the flow around the lifting surface. Previous unsteady ground effect studies have concluded that a stable equilibrium position exists at a distance away from the solid boundary that varies as a function of the Strouhal number [8]. We wish to probe the robustness of this conclusion by unlocking additional kinematic degrees-of-freedom and exploring a larger simulation parameter space.

It is important to emphasize how the roles of k and St change when considering a single versus multiple degree-of-freedom swimming condition. For a single, cross-stream degree-of-freedom simulation, k and St retain their roles as input parameters outlined in equations (2.10) and (2.11). However when the freestream degree-of-freedom in unlocked, St and k can no longer be prescribed. Rather, St and k shift roles and become output parameters contingent upon the steady-state, cycle-averaged freestream velocity of the propulsor, $\overline{U}$. For this reason, two parameter spaces are mapped out below in tables 2.1 and 2.2 for single and multiple degree-of-freedom swimming conditions, respec-

tively. The Strouhal number is now set indirectly by specifying the Lighthill number due to added drag effects in the freestream direction. In the same vain, the frequency is now held at a constant value of unity and the amplitude is varied in place of Strouhal number in the mutli-degree-of-freedom parameter sweep.

We wish to observe how varying the terms defined above effects a free swimming propulsor's equilibrium position and performance metrics. The full parameter space explored in this study is presented below for single and multi degree-of-freedom swimming conditions:

$\mathbf{m^*}$	$\mathbf{D_0^*}$	**k**	**St**	$\boldsymbol{\phi}$ **(deg.)**
3	0.25	0.5	0.2	0
10	0.50	1.0	0.35	180
20	0.75	2.0	0.50	-

Table 2.1: Parameter space for single degree-of-freedom simulations.

$\mathbf{m^*}$	$\mathbf{D_0^*}$	$\mathbf{A^*}$	$\boldsymbol{\theta}_0$**(deg.)**	$\boldsymbol{\phi}$ **(deg.)**	**Li**
3	0.25	0.25	7.81	0	0.3
10	0.50	0.5	14.48	180	-
20	0.75	0.75	22.02	-	-

Table 2.2: Parameter space for multi degree-of-freedom simulations.

2.2 Governing Equations

An unsteady, two dimensional potential flow method is used to model the flow around and study the performance of free swimming bio-inspired propulsors. The method begins with considering a stationary, undisturbed flow that is incompressible, inviscid, and irrotational everywhere except on the surface of the propulsor. As such, a scalar velocity potential can be said to exist such that:

$$\boldsymbol{u} = \boldsymbol{\nabla}\Phi \tag{2.12}$$

where $\boldsymbol{u}$ represents the velocity vector field within a stationary inertial reference frame denoted by (X, Z). The scalar velocity potential, Φ, defined within this stationary frame will be refereed to as the perturbation potential. The incompressible nature of the flow allows one to apply the simplified continuity equation:

$$\boldsymbol{\nabla} \cdot \boldsymbol{u} = 0 \tag{2.13}$$

Substituting equation (2.13) into equation (2.12) yields the familiar Laplace's Equation acting on the perturbation potential:

$$\boldsymbol{\nabla}^2\Phi = 0 \tag{2.14}$$

The quantities of interest for studying bio-inspired propolsors derive from solving equation 2.14 for the perturbation potential within the fluid domain. Once the perturbation potential is obtained, we may apply the unsteady Bernoulli

equation to solve for the pressure distribution throughout the fluid:

$$P_b(X, Z, t) = -\rho \frac{\partial \Phi}{\partial t}\bigg|_{X,Z} - \rho \frac{(\boldsymbol{\nabla}\Phi)^2}{2} \tag{2.15}$$

A Cartesian, body-fixed Lagrangian frame of reference is defined, denoted by (x, z), to aid in calculating the pressure acting on the body. We allow the propulsor to initially translate in the $-X$ direction with a with a body-fixed reference velocity, $\boldsymbol{U_0}$. A relative velocity, $\boldsymbol{u_r}$, is now defined to link the separate coordinate systems. We may now express the pressure field around the body in terms of the Lagrangian coordinate system local to the body:

$$P_b(x, z, t) = -\rho \frac{\partial \Phi}{\partial t}\bigg|_{x,z} + \rho(\boldsymbol{U_0} + \boldsymbol{u_r}) \cdot \nabla\Phi - \rho \frac{(\nabla\Phi)^2}{2} \tag{2.16}$$

The pressure may now be integrated around the body to calculate the total force vector, $\boldsymbol{F}$:

$$\boldsymbol{F}(t) = \int_{\mathcal{S}_b} -P_b \, \hat{\boldsymbol{n}} \, d\mathcal{S} \tag{2.17}$$

where $\mathcal{S}_b$ defines the body surface, $\hat{\boldsymbol{n}}$ the body surface unit normal vector, and $\hat{\boldsymbol{x}}$ a unit vector pointing in the positive x direction dictated by the body-fixed coordinate system. This total force vector may then be decomposed into its constituent components within the body-fixed frame to quantify classical quantities of interest, lift and thrust:

$$L(t) = F_z(t) \tag{2.18}$$

$$T(t) = -F_x(t) \tag{2.19}$$

A net-thrust equation is now defined due to the presence of a virtual body and its accompanying drag force:

$$T(t)_{net} = T(t) - D(t) \tag{2.20}$$

It is also useful to define the power that was input to the fluid by the propulsor. Power is defined as the integration over the boundary of the propulsor of the vector product of the negative local force times the local velocity:

$$P(t) = -\oiint_{\mathcal{S}_b} \boldsymbol{F} \cdot \boldsymbol{u_r}\, d\mathcal{S}_0 \tag{2.21}$$

where $\mathcal{S}_b$ represents the propulsor's body area and $d\mathcal{S}_0$ an infinitesimal body area.

It is often helpful to cast the forces and input power results into a non-dimensional form. Lift and thrust are normalized by the dynamic pressure and defined as such:

$$C_L = \frac{L(t)}{\frac{1}{2}\rho U_0^2 c} \tag{2.22}$$

$$C_T = \frac{T(t)}{\frac{1}{2}\rho U_0^2 c} \tag{2.23}$$

$$C_{T,net} = \frac{T_{net}(t)}{\frac{1}{2}\rho U_0^2 c} \tag{2.24}$$

Conversely, power is normalized by the dynamic pressure multiplied by the reference self-propulsion speed in the stream-wise direction, U_0:

$$C_P = \frac{P(t)}{\frac{1}{2}\rho U_0^3 c} \tag{2.25}$$

One may measure the efficiency of a propulsor by dividing the coefficient of thrust by the coefficient of power, equivalent to the ratio of useful power output to power input:

$$\eta = \frac{C_T}{C_P} \tag{2.26}$$

The metrics defined above are instantaneous measures and can be calculated at any moment in time. However, these metrics may be averaged over one complete pitching cycle to obtain an average performance metric. These averaged values will be denoted with the inclusion of an over-bar character.

2.3 Derivation of Boundary Integral Equation

Two boundary conditions must be set for the problem to be properly defined due to the governing equation being of order two. A zero-flux potential condition is enforced along the surface of the body:

$$\hat{\boldsymbol{n}} \cdot \boldsymbol{\nabla}\Phi - \hat{\boldsymbol{n}} \cdot (\boldsymbol{U_0} + \boldsymbol{u_r}) = 0 \tag{2.27}$$

In addition, any disturbances in the fluid caused by the body's propulsion must decay to zero infinitely far away:

$$\boldsymbol{\nabla}\Phi\Big|_{(x,z)\to\infty} = 0 \tag{2.28}$$

We now seek a general solution to equation (2.14). To do so, one must consider the potential response at an arbitrary point within the body-fixed reference frame $\boldsymbol{r} = [x, z]^T$ caused by a point source singularity located at point $\boldsymbol{r_0} =$

$[x_0, z_0]^T$. In doing so, we invoke the infinite space Green's Function in two dimensions:

$$G(\boldsymbol{r}; \boldsymbol{r_0}) = \frac{1}{2\pi} \ln |\boldsymbol{r} - \boldsymbol{r_0}| \tag{2.29}$$

We now use Green's Second identity with respect to equation (2.29) and the interior perturbation potential of the body, Φ_i, to formulate a boundary integral equation (BIE) representation of the problem:

$$\Phi_i(\boldsymbol{r}) = \oiint_{\mathcal{S}} [\hat{\boldsymbol{n}} \cdot \boldsymbol{\nabla}(\Phi - \Phi_i)\, G(\boldsymbol{r}; \boldsymbol{r_0}) + (\Phi - \Phi_i)\, \hat{\boldsymbol{n}} \cdot \boldsymbol{\nabla} G(\boldsymbol{r}; \boldsymbol{r_0})]\, d\mathcal{S}_0 \tag{2.30}$$

In order to allow for the introduction of a wake-shedding model, the surface $\mathcal{S}$ is broken up into two distinct surfaces, $\mathcal{S}_b$ and $\mathcal{S}_w$, to distinguish between the body surface and wake surface, respectively. The wake is modeled as a surface with zero thickness, leading the perturbation potential to be discontinuous across it. As such, the potential gradient term in the boundary integral representation of the wake evaluates to zero. Equation (2.30) can now be written as

$$\begin{aligned} \Phi_i(\boldsymbol{r}) = &\oiint_{\mathcal{S}_b} [\hat{\boldsymbol{n}} \cdot \boldsymbol{\nabla}(\Phi - \Phi_i)\, G(\boldsymbol{r}; \boldsymbol{r_0}) + (\Phi - \Phi_i)\, \hat{\boldsymbol{n}} \cdot \boldsymbol{\nabla} G(\boldsymbol{r}; \boldsymbol{r_0})]\, d\mathcal{S}_0 \\ &+ \oiint_{\mathcal{S}_w} [(\Phi - \Phi_i)\, \hat{\boldsymbol{n}} \cdot \boldsymbol{\nabla} G(\boldsymbol{r}; \boldsymbol{r_0})]\, d\mathcal{S}_0 \end{aligned} \tag{2.31}$$

The potential gradient and difference gradient terms above correspond to the singularity elements known as sources and doublets, respectively, possessing a

local strength denoted by σ and μ:

$$\sigma(\boldsymbol{r_0}) = \hat{\boldsymbol{n}} \cdot \boldsymbol{\nabla}(\Phi - \Phi_i) = -\frac{\partial \Phi}{\partial n} + \frac{\partial \Phi_i}{\partial n} \tag{2.32}$$

$$-\mu(\boldsymbol{r_0}) = \Phi - \Phi_i \tag{2.33}$$

Rewriting equation (2.31) in terms of these singularity elements, we obtain:

$$\begin{aligned} \Phi_i(\boldsymbol{r}) = & \oiint_{\mathcal{S}_b} \left[\sigma(\boldsymbol{r_0})\, G(\boldsymbol{r};\boldsymbol{r_0}) - \mu(\boldsymbol{r_0})\, \hat{\boldsymbol{n}} \cdot \boldsymbol{\nabla} G(\boldsymbol{r};\boldsymbol{r_0})\right] d\mathcal{S}_0 \\ & - \oiint_{\mathcal{S}_w} \left[\mu_w(\boldsymbol{r_0})\, \hat{\boldsymbol{n}} \cdot \boldsymbol{\nabla} G(\boldsymbol{r};\boldsymbol{r_0})\right] d\mathcal{S}_0 \end{aligned} \tag{2.34}$$

where μ_w represents the perturbation potential jump between the top and bottom of the wake surface:

$$-\mu_w(\boldsymbol{r_0}) = \Phi_+ - \Phi_- \tag{2.35}$$

2.4 Boundary Conditions and their Application

The problem is now reduced to finding a distribution of source and doublet elements over a body surface $\mathcal{S}_b$ and doublet elements over a wake surface $\mathcal{S}_w$. These singularity elements automatically satisfy the far field boundary condition (equation (2.28)) and therefore only need to be selected to ensure zero potential flux (equation (2.27)). This is done by stipulating a constant

perturbation potential within the body $\Phi_i = 0$, dictating the source strength on the body

$$\sigma_b = \hat{\boldsymbol{n}} \cdot \boldsymbol{\nabla}\Phi_b = \hat{\boldsymbol{n}} \cdot (\boldsymbol{U_0} + \boldsymbol{u_r}) \tag{2.36}$$

and doublet strength on the body

$$-\mu_b = \Phi_b \tag{2.37}$$

Substituting the zero interior potential boundary condition and definition of the Green Function into the original boundary integral equation on interior perturbation potential yields:

$$\begin{aligned} 0 = \frac{1}{2\pi}\Bigg[&\oiint_{\mathcal{S}_b} \left[\sigma(\boldsymbol{r_0}) \ln|\boldsymbol{r} - \boldsymbol{r_0}| - \mu(\boldsymbol{r_0}) \frac{\partial}{\partial n} \ln|\boldsymbol{r} - \boldsymbol{r_0}|\right] d\mathcal{S}_0 \\ &- \oiint_{\mathcal{S}_w} \mu_w(\boldsymbol{r_0}) \frac{\partial}{\partial n} \ln|\boldsymbol{r} - \boldsymbol{r_0}| \, d\mathcal{S}_0 \Bigg] \end{aligned} \tag{2.38}$$

2.5 Numerical Solution to the Boundary Integral Equation

We now seek to numerically solve equation (2.38) by approximating the body and wake surfaces to be integrated over. Following [34], the continuous body surface $\mathcal{S}_b$ is discretized into N_b body panels and the continuous wake surface $\mathcal{S}_w$ into N_w wake panels. The body is discretized using both source and doublet panels to allow for the simulation of a thick lifting body [34] whereas the wake is comprised of only doublet panels. We also enforce a constant strength over

each panel's length:

$$\sigma(x_p) = \sigma = const. \tag{2.39}$$

$$\mu(x_p) = \mu = const. \tag{2.40}$$

The streamlines associated with these singularity panels are presented below in figure 2.2:

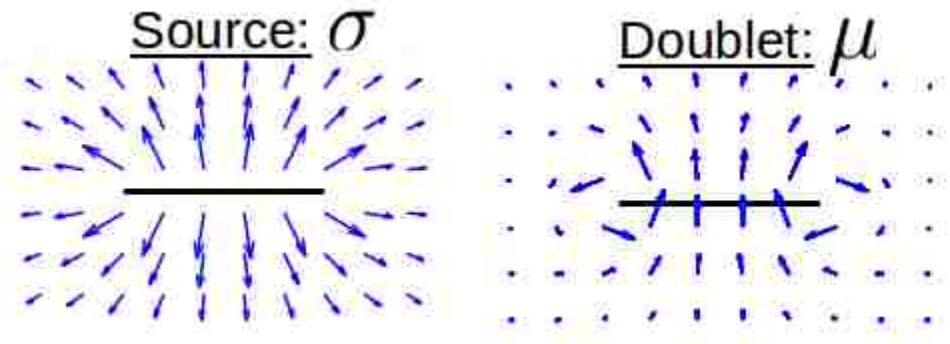

Figure 2.2: Streamlines of source and doublet panels.

The distribution of source and doublet panels on the body of interest follows a cosine distribution. This is done to ensure the curved and thin aspects of the geometry receive adequate resolution at the leading and trailing edges and therefore a more accurate representation of the body. A standard cosine panel distribution is shown below in figure 2.3:

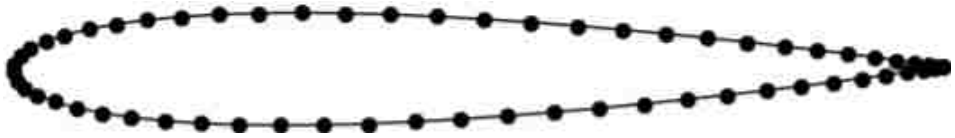

Figure 2.3: NACA 0012 airfoil with a singularity body panel configuration following a cosine distribution. The concentration of body panels is larger at the leading and trailing edges to ensure reasonable surface resolution.

The constant interior potential boundary condition is now enforced at a single collocation point for each boundary element. The collocation point is located at the midpoint of the panel, shifted into the body by 10% of the local body thickness along the panel's unit normal vector. Integration is then carried out locally over each panel to approximate the surfaces of interest. We may rewrite equation (2.38) to reflect its approximate nature in a discrete matrix representation:

$$\sum_{j=1}^{N_b} B_{ij}\sigma_j + \sum_{j=1}^{N_b} C_{ij}\mu_j + \sum_{k=1}^{N_w} C_{w,ik}\mu_{w,k} = 0 \tag{2.41}$$

where B_{ij}, C_{ij}, and $C_{w,ik}$ are influence coefficients defined by:

$$B_{ij} = \frac{1}{2\pi}\int_{panel} \ln|\boldsymbol{r_i} - \boldsymbol{r_{0,j}}|\, d\mathcal{S}_0 \tag{2.42}$$

$$C_{ij} = -\frac{1}{2\pi}\int_{panel} \frac{\partial}{\partial n}\left(\ln|\boldsymbol{r_i} - \boldsymbol{r_{0,j}}|\right) d\mathcal{S}_0 \tag{2.43}$$

$$C_{w,ik} = -\frac{1}{2\pi}\int_{panel} \frac{\partial}{\partial n}\left(\ln|\boldsymbol{r_i} - \boldsymbol{r_{0,k}}|\right) d\mathcal{S}_0 \tag{2.44}$$

where $d\mathcal{S}_0$ is the differential length of a boundary element (panel). The first index of an influence coefficient corresponds to the influencing element whereas

the second index corresponds to its target. The vectors r_i and $r_{0,j}$ define the location of the ith target panel's collocation point and jth influencing panel's collocation point. The integrals seen in equations (2.42) - (2.44) have analytical solutions when the coordinates are cast into a panel oriented coordinate system as seen in figure 2.4. For example, consider the the perturbation potential induced by a constant strength source distribution at an arbitrary point P:

$$\Phi(x,z) = \frac{\sigma}{2\pi}\int_{x_{p1}}^{x_{p2}} \ln\sqrt{(x-x_0)^2+z^2}\; dx_0 \tag{2.45}$$

Before we evaluate the result, x and z are transformed by the rotation matrix presented in equation (2.46):

$$\begin{pmatrix} x \\ z \end{pmatrix}_p = \begin{pmatrix} cos\,\alpha_i & -sin\,\alpha_i \\ sin\,\alpha_i & cos\,\alpha_i \end{pmatrix} \begin{pmatrix} x-x_0 \\ z-z_0 \end{pmatrix} \tag{2.46}$$

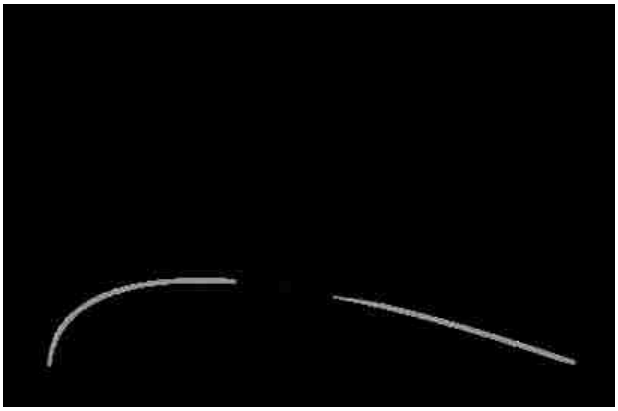

Figure 2.4: Panel based coordinate system that results from rotation matrix applied to global coordinate system.

where the subscript p denotes a panel frame coordinate system and the sub-

script 0 denotes a panel's origin with reference to the inertial frame. It is important to note that the variable x_0 in equation (2.45) is simply a dummy variable utilized for integration purposes and has no relation to the panel's coordinate origin.

The integral presented in equation (2.45) has the following solution where x and z are measured with reference to the local panel coordinate system:

$$\Phi(x,z) = \frac{\sigma}{4\pi}\Bigg\{(x-x_{p1})\,\ln[(x-x_{p1})^2+z^2] - (x-x_{p2})\,\ln[(x-x_{p2})^2+z^2] \\ -2(x_{p2}-x_{p1}) + 2z\left(\tan^{-1}\frac{z}{x-x_{p2}} - \tan^{-1}\frac{z}{x-x_{p1}}\right)\Bigg\} \tag{2.47}$$

Similarly, the doublet induced potential at an arbitrary point is found by the following integral:

$$\Phi(x,z) = \frac{-\mu}{2\pi}\int_{x_{p1}}^{x_{p2}} \frac{z}{(x-x_0)^2+z^2}\,dx_0 \tag{2.48}$$

The solution, presented in panel coordinates, is found to be:

$$\Phi(x,z) = \frac{-\mu}{2\pi}\left[\tan^{-1}\frac{z}{x-x_{p2}} - \tan^{-1}\frac{z}{x-x_{p1}}\right] \tag{2.49}$$

The problem presented thus far possesses an influence coefficient matrix that is of size $N \times N$ (corresponding to N singularity panels with N collocation points) with N unknowns (doublet panel strengths).

To support the shedding of vorticity into the wake an additional singularity

panel must be added to the trailing edge of the geometry of interest. We now introduce a trailing edge doublet element which is the first in the set of wake elements. This element is oriented such that it bisects its adjacent panels. The length of this element is typically a function of the magnitude body-fixed reference velocity, U_0 [35]:

$$L_{TE} = 0.4\, U_0\, \Delta t \tag{2.50}$$

where Δt is the length of a discrete time step. The trailing edge singularity strength, the $(N+1)$th unknown, is dictated by the difference in doublet panel strengths above and below the element:

$$\mu_{w,TE} = \mu_{t,TE} - \mu_{b,TE} \tag{2.51}$$

This condition is classically referred to as an explicit Kutta condition and ensures a finite velocity at the trailing edge of the propulsor. In other words, this condition provides the additional known needed to solve the matrix representation of the boundary integral equation. The explicit Kutta condition was chosen over an implicit variant due to its ease of implementation and physical adequacy at modest kinematic maneuvers. We may reduce the order of the now $(N + 1 \times N + 1)$ influence matrix back to its native $(N \times N)$ size by rewriting the trailing edge element's strength in terms of body element doublet strengths. Moving known quantities to the right hand side and redefining the influence coefficient associated with the doublet panels, we obtain:

$$\sum_{j=1}^{N_b} A_{ij}\mu_j = -\sum_{j=1}^{N_b} B_{ij}\sigma_j - \sum_{k=2}^{N_w} C_{w,ik}\mu_{w,k} \tag{2.52}$$

where A_{ij} is defined by:

$$A_{ij} = \begin{cases} C_{ij} - C_{w,i1}, & \text{j = bottom panel} \\ C_{ij} + C_{w,i1}, & \text{j = top panel} \\ C_{ij}, & \text{otherwise} \end{cases} \tag{2.53}$$

With coefficient matrices A_{ij}, B_{ij}, and $C_{w,ik}$ fully defined and singularity strengths σ_j and $\mu_{w,k}$ known, we may invert matrix A_{ij} to solve for the unknown body doublet panel strengths, μ_j, to satisfy the boundary condition presented in equation (2.27). The perturbation potential on the surface of the body may now be solved for as the jump in potential across the solid boundary:

$$\Phi_s = \Phi_i - \mu_j = -\mu_j \tag{2.54}$$

Steady forces and loads may now be calculated in accordance with equations (2.16) and (2.17). To solve for the unsteady body loading, however, one must consider the implementation of a wake shedding model and the change of perturbation potential over time.

2.6 Wake Model

The potential flow analysis presented thus far has not possessed a temporal component. Although the continuity equation (and by association Laplace's Equation) is independent of time, a time-dependent boundary condition and complementary wake-shedding model is implemented to study the evolution

of the potential flow solution and wake structure over time. This formulation enables the unsteady Bernoulli equation (2.16) to be utilized without issue.

Kelvin's circulation theorem states that the circulation around an arbitrary closed contour moving with a body and wake must remain constant in time:

$$\frac{\mathrm{D}\Gamma}{\mathrm{D}t} = 0 \tag{2.55}$$

where the circulation, Γ, is defined by

$$\Gamma = \oint_C \boldsymbol{u} \cdot d\boldsymbol{l} \tag{2.56}$$

In order to satisfy Kelvin's Circulation theorem, the bound circulation of the body is canceled with a doublet panel of equal but opposite circulation. At every time step, the trailing edge wake panel is "shed" into the wake with strength equal to $\mu_{w,TE}$, allowing a new doublet wake trailing edge element to be formed during the next time step. The shed doublet panel is advected a distance $U_0 \Delta t$ along its unit tangent vector and maintains its strength as it propagates down stream. There is no decay of vorticity due to the absence of viscous and compressible effects in this potential flow formulation. The wake doublet panels are further advected by the local induced velocity field from other doublet panels (both body and wake). Seeing as doublet panels are mathematically equivalent to two point vortices of opposite circulations located at the panel endpoints [34], the induced velocity is calculated by employing a

de-singularized variant of the Biot-Savart law [36]:

$$\boldsymbol{u}(\boldsymbol{r}) = \frac{\Gamma}{2\pi} \frac{\hat{\boldsymbol{s}} \times (\boldsymbol{r} - \boldsymbol{r_i})}{|\boldsymbol{r} - \boldsymbol{r_i}|^2 + \delta^2} \tag{2.57}$$

The de-singularization parameter δ is utilized to avoid infinite induction as the distance between induction-pair singularity elements approaches zero. In this analysis, a δ/c value of 1×10^{-2} is used as it yielded the best results during validation testing. Additionally, Γ represents an equivalent point vortex circulation for a given doublet panel strength.

A lengthier and more laborious influence calculation must be performed for every wake element shed. To reduce the growth of the problem we impose an upper limit on the number of wake elements that may exist in the domain at a given time. After this limit is reached, the wake element that was the first to be shed (and is now furthest downstream) will absorb its adjacent wake element as a new element is shed from the trailing edge of the body. This modified wake element is now referred to as a lumped vortex. The lumped vortex approximates the fully resolved wake and grows increasingly accurate as the maximum number of wake elements allowed to exist in the computational domain increases. The position and circulation values of this modified wake element are calculated using a weighted average [37]:

$$\Gamma^n_{lump} = \Gamma^{n-1}_{lump} + \Gamma^n_{w,absorbed} \tag{2.58}$$

$$\boldsymbol{p}^n_{lump} = \left[\frac{\Gamma^{n-1}_{mag}}{\Gamma^n_{mag}}\right] \boldsymbol{p}^{n-1}_{lump} + \left[\frac{|\Gamma^n_{w,absorbed}|}{\Gamma^n_{mag}}\right] \boldsymbol{p}^n_{absorbed} \tag{2.59}$$

where $\Gamma^n_{mag} = \Gamma^{n-1}_{mag} + |\Gamma^n_{w,absorbed}|$, n is the current time step, $n-1$ is the previous time step, and $\boldsymbol{p}$ is the vector position of a wake element. In the free swimming simulations, the number of fully resolved cycles, N_{Lump}, was continuously doubled until the time-averaged, steady-state leading edge trajectory solutions changed by less than 1%. A cycle limit of $N_{Lump} = 8$ met this criteria and was deemed sufficient to maintain solution accuracy and reduce computational cost.

In order to observe the evolution of the wake and its ground interaction over time, the solution space within the computational domain is plotted at each time step:

Figure 2.5: At each time step a wake element is shed from the propulsor's trailing edge into the computational domain. Each scatter point corresponds to a doublet wake panel's endpoint. The wake elements are colored to reflect its strength and rotation.

The colored scatter points shed from the hydrofoil's trailing edge represent a wake element. The range of wake element strengths present in the field are then mapped onto a red-blue color bar gradient. A wake element with positive strength is colored red and rotates counterclockwise. Conversely, a negative

strength element is colored blue and rotates counterclockwise.

With the wake model defined and the unsteady portion of problem detailed, the unsteady versions of equations (2.16) and (2.17) can now be utilized to calculate the unsteady loading acting on the body.

2.7 Solution Convergence

Due to the discrete representation of the boundary integral equation (2.52), we must ensure that a sufficient number of spacial and temporal discretization elements are utilized in the simulations. The number of source and doublet body panels, N_b, and number of time steps per pitching cycle, N_s, were systematically doubled independently to observe the impact they had on the problem's steady state solution. Steady state is considered to be achieved when the hydrofoil's cycle-averaged D^* value, $\overline{D}^*$, changed by less than 3%. The current study only considered $\overline{D}^*$ as a convergence metric, as the hydrofoil's averaged trajectory is a good indicator for the convergence of other performance metrics such as $\overline{C}_L$ and $\overline{\eta}$. The convergence study results, seen in figure 2.6, indicate that the steady state solution changes by less than 2% for $N_b = 250$ and $N_s = 250$ and thus provide adequate resolution to the discrete problem at hand.

2.8 Validation

To verify that the solving methodology employed is sound and the discretized boundary integral equation is being solved correctly, we compare against the results of Theodorson [38] and Garrick [39]. Theodorson produced an ana-

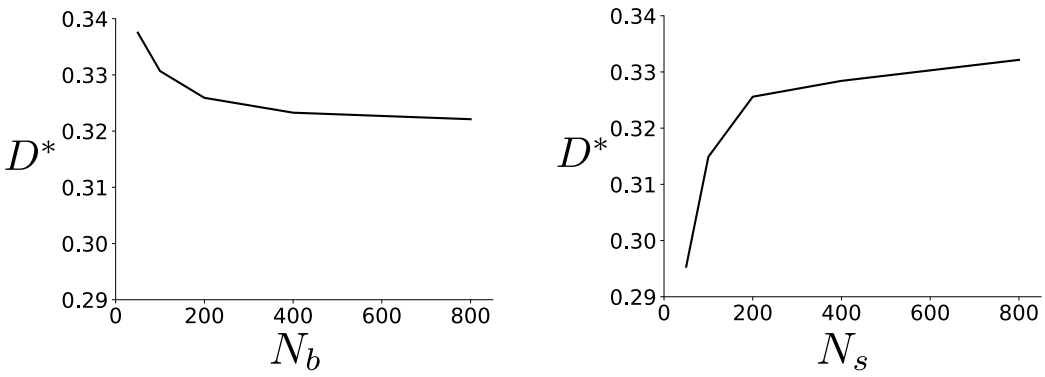

Figure 2.6: Convergence of trajectory with increasing spacial and temporal resolution.

lytical model for the lift acting upon a pitching and heaving airfoil, whereas Garrick expanded upon this theory to find the thrust and input power. The assumptions involved in the analytical theory include a thin airfoil undergoing small amplitude harmonic motion with a planar and non-deforming wake. The potential flow solver accounts for the non-deforming wake assumption by omitting the de-singularized Biot-Savart calculations seen in equation (2.57). Analytical solutions for the lift, thrust, and power coefficients exhibited by a hydrofoil undergoing pure pitching about its leading edge are reproduced below:

$$C_L^T = \frac{1}{2}\left[\dot{\alpha} + \frac{1}{2}\ddot{\alpha}\right] + 2\left[\alpha + \frac{3}{4}\dot{\alpha}\right]C(k) \tag{2.60}$$

$$C_T^G = \frac{3\pi^3}{32} - \frac{\pi^3}{8}\left[\frac{3F}{2} - \frac{G}{2\pi k} + \frac{F}{\pi^2 k^2} - (F^2+G^2)\left(\frac{1}{\pi^2 k^2} + \frac{9}{4}\right)\right] \tag{2.61}$$

$$C_P^G = \frac{3\pi^3}{32} + \frac{\pi^3}{16}\left[\frac{3F}{2} + \frac{G}{2\pi k}\right] \tag{2.62}$$

where the T and G superscripts denote Theodorson's and Garrick's results, respectively. $C(k)$ is referred to as Theodorson's lift deficiency function [38] and is comprised of a real (F) and imaginary (G) part:

$$F(k) = \frac{J_1(J_1 + Y_0) + Y_1(Y_1 - J_0)}{(J_1 + Y_0)^2 + (Y_1 - J_0)^2} \tag{2.63}$$

$$G(k) = -\frac{Y_1 Y_0 + J_1 J_0}{(J_1 + Y_0)^2 + (Y_1 - J_0)^2} \tag{2.64}$$

where J_0, J_1, Y_0, and Y_1 are Bessel Functions of the first and second kind, respectively. In addition, α defines the instantaneous pitching angle of the foil:

$$\alpha = \theta_0 \sin(2\pi f t + \phi) \tag{2.65}$$

The time derivative terms in equation (2.60) simply equal:

$$\dot{\alpha} = 2\pi f \theta_0 \cos(2\pi f t + \phi) \tag{2.66}$$

$$\ddot{\alpha} = -4\pi^2 f^2 \theta_0 \sin(2\pi f t + \phi) \tag{2.67}$$

It is important to note for validation purposes the force and power coefficients produced by the potential flow solver are now non-dimensionalized using the added-mass forces and added-mass power to align with Theodorson's and Garrick's linear theory:

$$C_L = \frac{L}{\rho c f^2 A^2} \tag{2.68}$$

$$C_T = \frac{T}{\rho c f^2 A^2} \tag{2.69}$$

$$C_P = \frac{P}{\rho c f^2 A^2 U_0} \tag{2.70}$$

These solutions are then plotted alongside the results of the potential flow solver for a reduced frequency of 1.0 and 0.1 in figure 2.7:

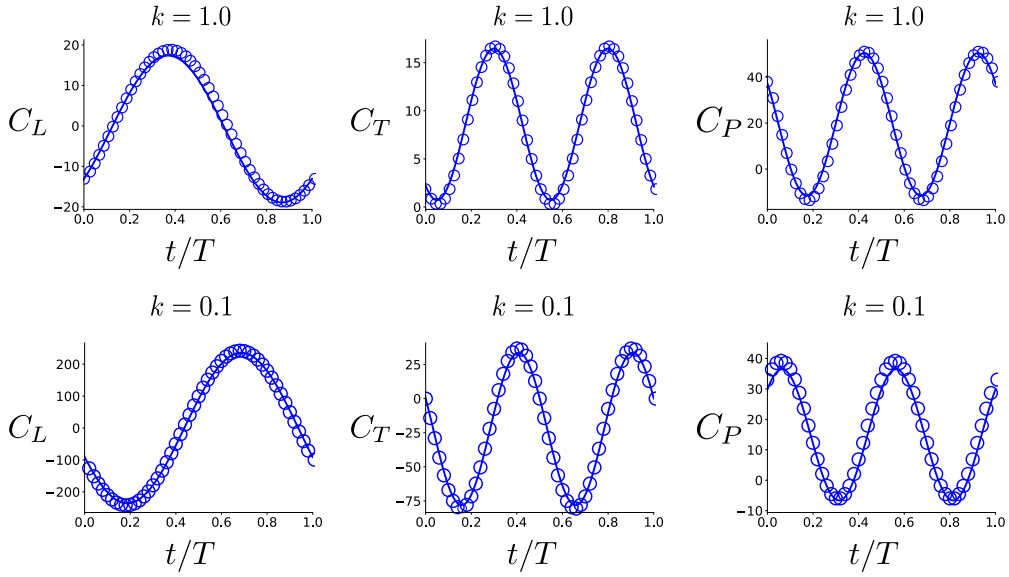

Figure 2.7: Comparison of potential flow solver solution with analytical solution. Solid line (-) corresponds to the analytical solution and scatter points (o) correspond to the potential flow solver solution. t/T is normalized time.

The maximum instantaneous error for all metrics was found to be less than 2% for all reduced frequencies tested and suggests the solver is functioning properly.

2.9 Implementation of the Solid Boundary

To model the presence of the ground, an additional boundary condition of zero flux through the ground plane must be satisfied:

$$w\Big|_{z=0} = 0 \tag{2.71}$$

where w is the fluid's lateral component of velocity, normal to the ground plane. This boundary condition can be satisfied by employing a method of images. An image propulsor is modeled within the computational domain that mirrors the kinematics of the real propulsor. The image swimmer is prescribed identical pitching kinematics as the body of interest with the addition of a phase delay of 180°. To accommodate multiple swimmers in the computational domain, one must consider the image's body panel and wake panel influences when constructing the influence matrices in equation (2.52) and performing wake induced velocity calculations in accordance with equation (2.57). The result is a no-penetration ground plane equidistant from either propulsor seen in figure 2.8:

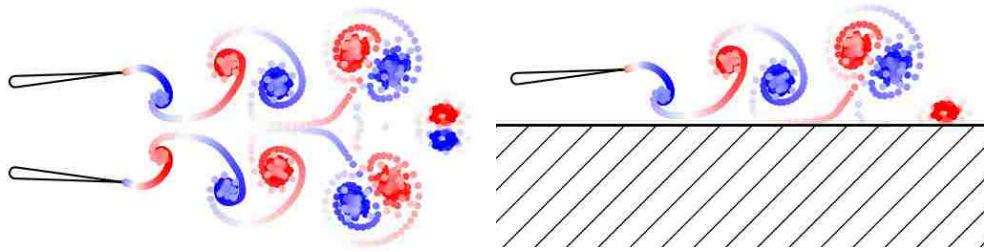

(a) (b)

Figure 2.8: A zero flux ground plane is created via the method images. (a) Two propulsor's are placed within the computational domain with out-of-phase pitching kinematics to create a symmetry plane at $z = 0$. This automatically satisfies the no-flux boundary condition. (b) The resulting equivalent representation of the multi-body problem is akin to a single propulsor swimming near a solid boundary.

2.10 Free Swimming Implementation

In order to allow for a more realistic model of a bio-propulsor, we follow [40] by implementing kinematic equations of motion that are loosely coupled into the potential flow solver. The cross-stream and/or freestream velocities are updated at every time step using a forward differencing scheme depending on which degrees-of-freedom are unlocked:

$$W^{n+1} = W^n + \frac{F_z^n}{m}\Delta t \tag{2.72}$$

$$U^{n+1} = U^n + \frac{F_{x,net}^n}{m}\Delta t \tag{2.73}$$

The leading edge position of the hydrofoil is then updated by a simple trapezoidal rule:

$$z_b^{n+1} = z_b^n + \frac{1}{2}(W^{n+1} + W^n)\Delta t \tag{2.74}$$

$$x_b^{n+1} = x_b^n + \frac{1}{2}(U^{n+1} + U^n)\Delta t \tag{2.75}$$

The n and $n+1$ superscripts represent the current and next time steps, respectively.

Chapter 3

Results

3.1 Single Translational Degree of Freedom

We begin by observing the effect of initial pitch direction on the steady state position of a bio-inspired hydrofoil. The leading edge trajectories measured in terms of D^* are presented in figure 3.1 for a single simulation case of $St = 0.2$, $k = 0.5$, $m^* = 10$, and $D_0^* = 0.75$ with pitch direction varied:

It can be seen that a stable equilibrium position is achieved after approximately 50 pitching cycles for both pitch cases. Steady-state is defined as when the cycle-averaged coefficient of lift forces acting on the hydrofoil approach zero ($\overline{C}_L = \mathcal{O}(10^{-5})$). The pitching phase shift appears to only affect the transient component of the trajectory data. The leading edges then maintain identical cycle-averaged D^* values for the duration of the simulation.

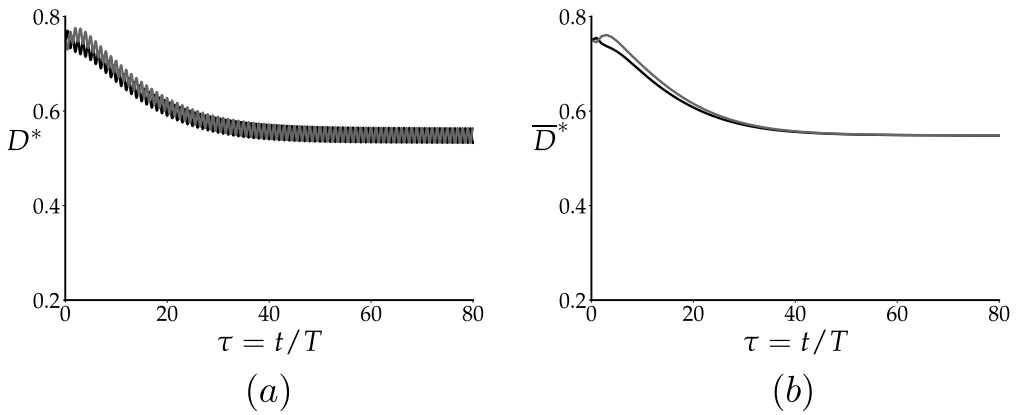

Figure 3.1: Trajectory data for hydrofoils with with $St = 0.2$, $k = 0.5$, $m^* = 10$, $D_0^* = 0.75$ for different initial pitching conditions. (a) Instantaneous leading-edge position (b) Cycle-averaged leading edge position. The dark and light lines correspond to a pitch-up and pitch-down condition, respectively.

We now present the results of initial pitch direction for the same simulation case of $St = 0.2$, $k = 0.5$, and $m^* = 10$ at all initial ground distances in figure 3.2. The hydrofoils are attracted to the same equilibrium location and are largely unaffected by their initial position. The smallest D_0^* case results in a positive lift force due to ground proximity and pushes the hydrofoil away from the boundary. Larger D_0^* values result in negative lift, pulling the hydrofoil towards the boundary. The equilibrium location coincides with the lateral position where the time-averaged lift force switches sign and the lateral velocity is sufficiently small.

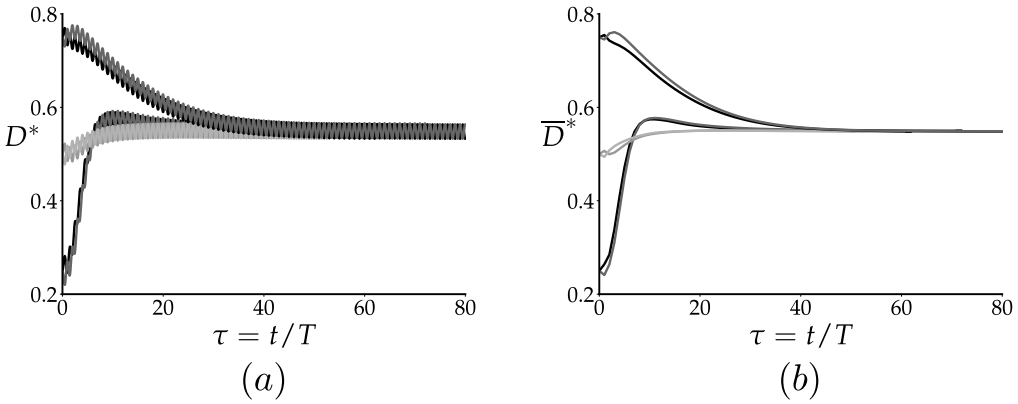

Figure 3.2: Trajectory data for hydrofoils with $St = 0.2$, $k = 0.5$, and $m^* = 10$ for different initial pitching conditions and lateral starting positions. (a) Instantaneous leading-edge position. (b) Cycle-averaged leading edge position. The dark and light lines correspond to a pitch-up and pitch-down condition, respectively.

It is worth noting that this equilibrium point is stable in the sense that perturbations away from the location will result in forces that draw the propulsor back. These findings coincide with those reported in [8], confirming that the implementation of a cross-stream degree-of-freedom does not alter the existence of stable equilibrium positions. The exception to this conclusion applies to extreme acceleration (small m^*) and large pitching amplitude cases that begin sufficiently close to the wall. The transient portion of the trajectory path grows unstable as a result of the propulsor intersecting the ground plane. The unstable trajectory data for $St = 0.2$, $k = 1.0$, $m^* = 3$, and $D_0^* = 0.25$ is presented in figure 3.3 for a single initial condition case. It can be seen that pitch down initial condition fails due to ground collision. The pitch up initial condition is attracted towards a stable equilibrium.

We now turn our attention to the wake structures developed by these differ-

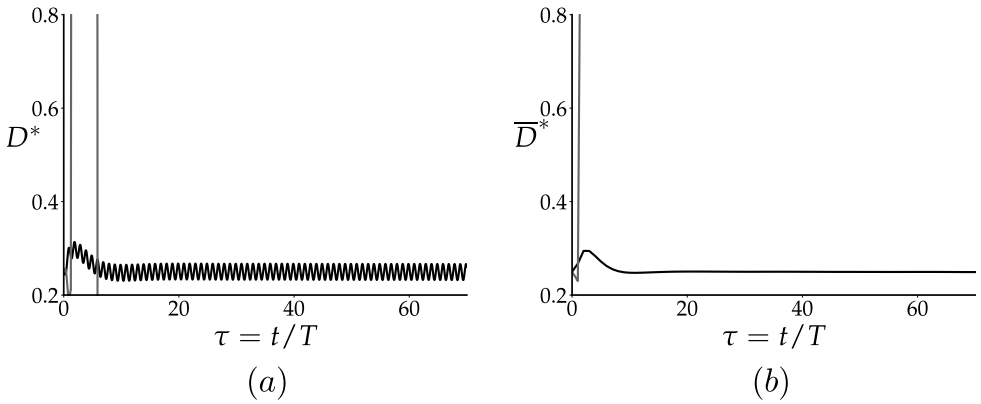

Figure 3.3: Unstable trajectory data for hydrofoils with $St = 0.2$, $k = 1.0$, $m^* = 3$, and $D_0^* = 0.25$ for different initial pitching conditions. (a) Instantaneous leading-edge position. (b) Cycle-averaged leading edge position. The dark and light lines correspond to a pitch-up and pitch-down condition, respectively.

ent swimming conditions. The propulsor forms vortex pairs for all swimming conditions considered. The typical 2S reverse von Kármán street observed in isolated swimming conditions is broken in favor of an angled vortex trajectory. These findings are consistent with [8]. The introduction of lateral propulsor movement, however, results in a gradual change in the vortex angle as the propulsor gravitates towards its equilibrium position. The wakes resulting from the hydrofoils analyzed in figure 3.2 are presented below in figure 3.4. It can be seen that the hydrofoils possess practically identical wake structures when steady-state propulsion is achieved, providing evidence for the claim that wake development is insensitive to initial condition.

We now consider identical St cases with a variation in body mass. The propulsion condition of $St = 0.2$, $k = 0.5$, and $D_0^* = 0.25$ is analyzed in figure 3.5 where we observe that varying the body mass has a noticeable affect

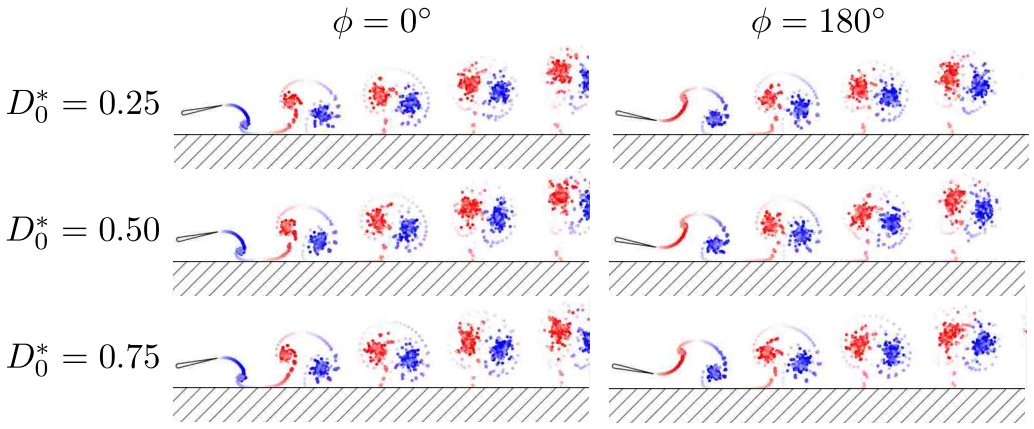

Figure 3.4: Wake structures corresponding to steady-state hydrofoils undergoing varying initial pitching conditions at all D_0^* values considered.

on equilibrium. Smaller m^* values appear to result in an equilibrium closer to the solid boundary. It is expected that as m^* becomes sufficiently large (approaching the static case presented in [37]) we will observe an equilibrium position identical to that reported in [37]. An additional insight can be gleamed by analyzing the instantaneous trajectory data in figure 3.5.

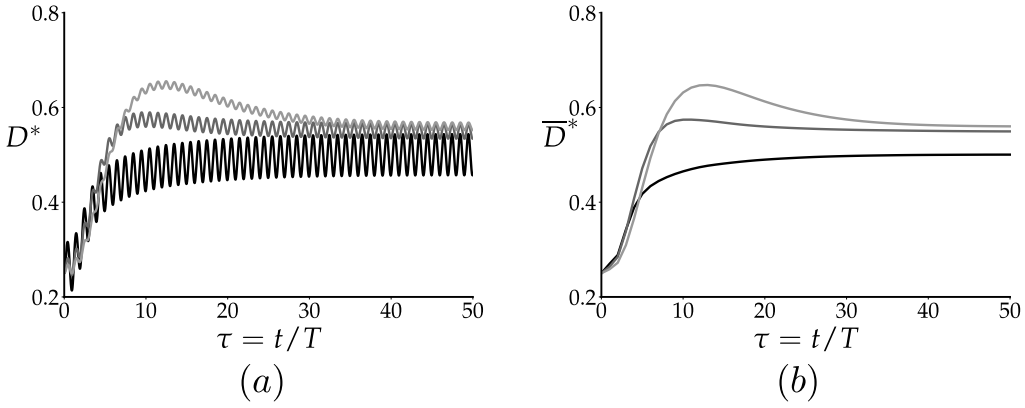

Figure 3.5: Trajectory data for hydrofoils with $St = 0.2$, $k = 0.5$, and $D_0^* = 0.25$ for different non-dimensional masses. (a) Instantaneous leading-edge position. (b) Cycle-averaged leading edge position. The line colors, from darkest to lightest, correspond to $m^* = 3, 10, 20$.

The oscillations appear to dampen out as the mass of the body increases. This makes intuitive sense, as a constant lift force acting on larger masses will produce smaller accelerations and therefore displacements. We hypothesize that the equilibrium position is a function of induced heave kinematics resulting from a given m^* value. The affect of non-dimensional mass becomes more prominent as the propulsor's St value is increased as seen in figure 3.6 for $St = 0.35$, $k = 1$, and $D_0^* = 0.50$:

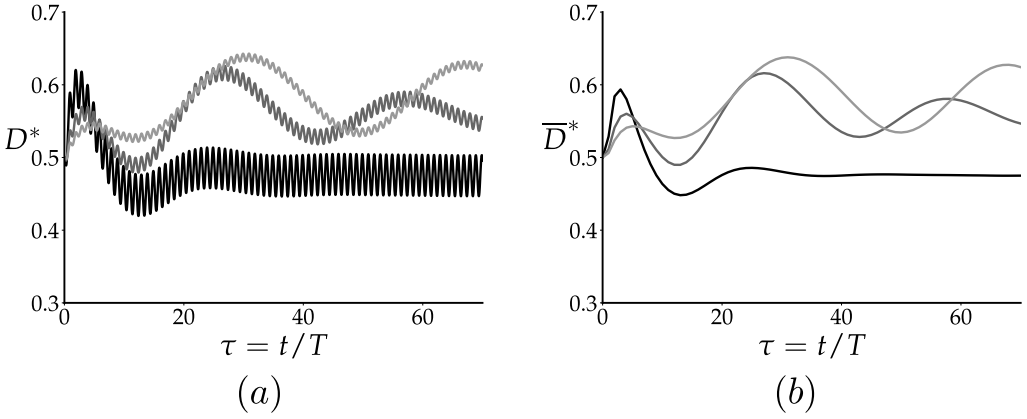

Figure 3.6: Trajectory data for hydrofoils with $St = 0.35$, $k = 1$, and $D_0^* = 0.50$ for different non-dimensional masses. (a) Instantaneous leading-edge position. (b) Cycle-averaged leading edge position. The line colors, from darkest to lightest, correspond to $m^* = 3, 10, 20$.

The hydrofoil's response becomes increasingly oscillatory and takes longer to converge to a steady-state value. We draw an analogy to a traditional mass-spring-damper system in that larger m^* values manifest as low damping coefficients. Similarly, m^* has an effect on the amplitude of oscillation and therefore similarly impacts an equivalent spring coefficient. Future research endeavors include taking sets of propulsor trajectory data and deriving

equivalent mechanical systems for performance prediction at a fraction of the computational cost.

The wake structures corresponding to the propulsion cases shown in figure 3.6 are shown in figure 3.7 below:

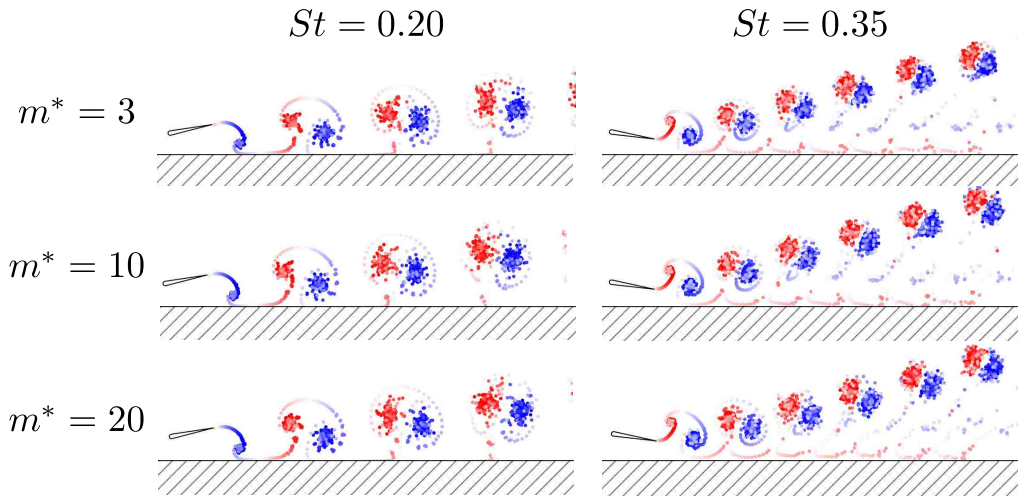

Figure 3.7: Wake structures corresponding to steady-state hydrofoils with varying non-dimensional masses for $St = 0.20, 0.35$.

As predicted, larger St values result in vortex pairs that are tightly packed in the wake. Varying the non-dimensional mass of a propulsor appears to change the angle of the vortex pair trajectory in the wake. Although the effect is marginal for the swimming condition presented in figure 3.7, it is hypothesized the angle change becomes more substantial for larger differences in m^*. The change in wake angle as a result of m^* appears to be slightly more prominent for larger St numbers. It is therefore proposed that lightweight propulsors undergoing large pitching motions (and therefore operating at large St numbers) will exhibit highly deflected wakes while in unsteady ground effect.

The performance metrics of $\overline{\eta}$ and $\overline{C}_T$ are now analyzed as the foil approaches its equilibrium position over time for the case presented in figure 3.5 of $St = 0.2$, $k = 0.5$, and $D_0^* = 0.25$ in figures 3.8 and 3.9.

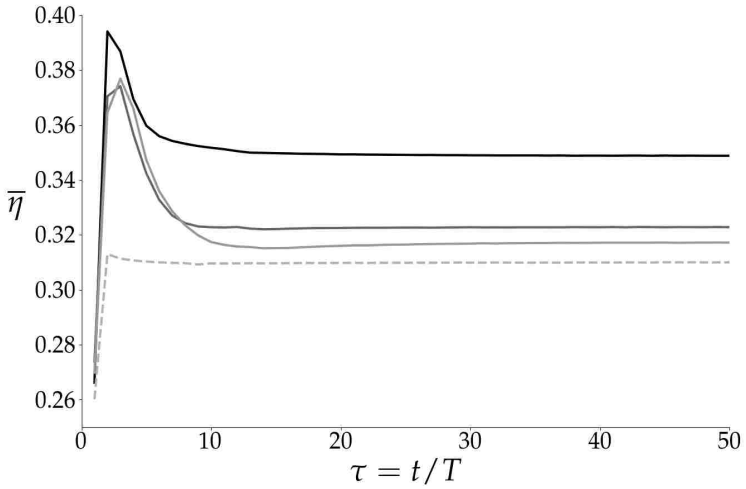

Figure 3.8: Cycle-averaged propuslive efficiency data for a hydrofoil with $St = 0.2$, $k = 0.5$, and $D_0^* = 0.25$ for varying m^* values. The line colors, from darkest to lightest, correspond to $m^* = 3, 10, 20$. The dashed line corresponds to a propulsor with infinite mass operating out of ground effect.

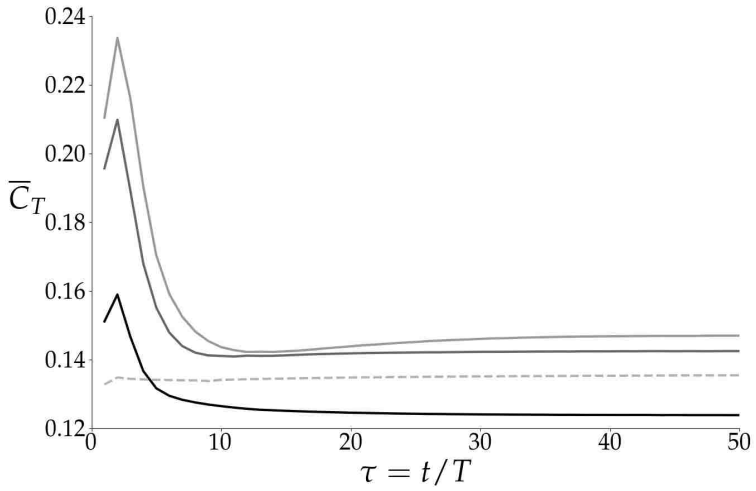

Figure 3.9: Cycle-averaged non-dimensional thrust data for a hydrofoil with $St = 0.2$, $k = 0.5$, and $D_0^* = 0.25$ for varying m^* values. The line colors, from darkest to lightest, correspond to $m^* = 3, 10, 20$. The dashed line corresponds to a propulsor with infinite mass operating out of ground effect.

For all cases considered, it appears that the hydrofoil propels itself more efficiently for smaller m^* values. Although the steady-state value only changes by ~4% for this particular case, it is a propuslive benefit that has not been identified in current ground effect literature. In addition, this small benefit may help shed light as to why many ground swimmers are comparatively small in size. It is worth noting that an additional thrust may be generated at the cost of efficiency for larger swimmers. We also plot the performance of a non-free swimming (infinite mass) propulsor out of ground effect with identical kinematics in figures 3.8 and 3.9 for reference.

We observe a similar performance trend for the thrust results in figure 3.9. It appears, however, that thrust generation is degraded as a result of unsteady ground effect for the smallest m^* value considered. As m^* increases, the ground

effect propulsor begins to outperform the isolated propulsor as a result of increased cycle-averaged steady state thrust. This finding seems to suggest that there exists a critical m^* value such that thrust generation for a propulsor in ground effect is identical to an isolated propulsor while the ground effect propulsor maintains a larger propulsive efficiency. We hypothesize that there is a non-dimensional mass threshold that must be surpassed to discern thrust benefits from unsteady ground effect. Future research endeavors include quantifying the non-dimensional mass of currently identified ground swimmers and evaluating if they fall within their respective critical mass regimes. Positive results may help justify the existence of particular ground swimmers.

We now examine the effect of varying St on the equilibrium position for the kinematics case of $k = 1.0$, $D_0^* = 0.25$, and $m^* = 3.0$. Trajectory data for all St values within the current parameter space is presented in figure 3.10:

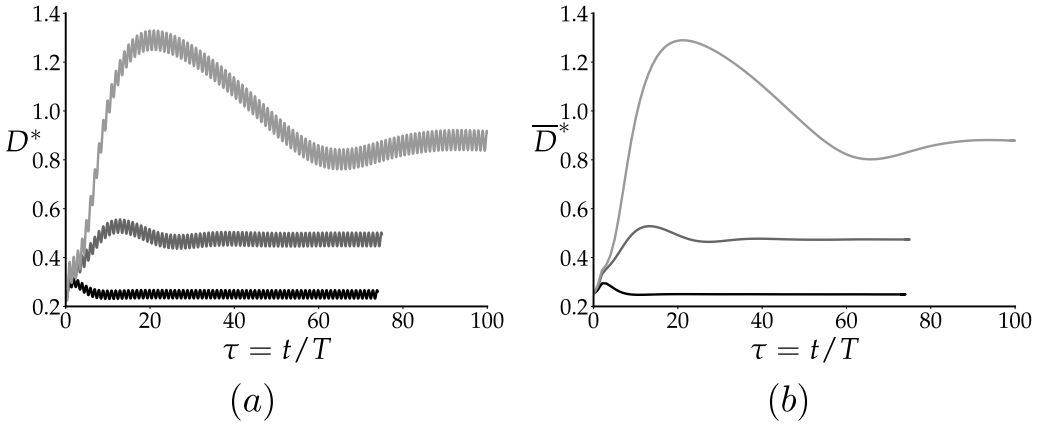

Figure 3.10: Trajectory data for hydrofoils with $k = 1.0$, $D_0^* = 0.25$, and $m^* = 3.0$ for different St values. (a) Instantaneous leading-edge position. (b) Cycle-averaged leading edge position. The line colors, from darkest to lightest, correspond to $St = 0.2, 0.35, 0.5$.

It can be clearly seen that changing St results in a different equilibrium position as predicted in [8]. Larger St values also seem to result in an increase in equilibrium location and convergence time. In addition, the instantaneous trajectory data suggests larger St values increase the amplitude of the leading-edge oscillations. It is theorized that small m^* values coupled with large St value kinematics will result in large amplitude leading edge trajectory oscillations.

The performance metrics, plotted in figures 3.11 and 3.12, also change considerably as a function of St. A larger St value, which corresponds to a larger pitching amplitude, results in larger time-averaged thrust values. This benefit occurs at the cost of lower propulsive efficiency. However, the decrease in efficiency can be regarded as fairly negligible when considering the return on thrust increase.

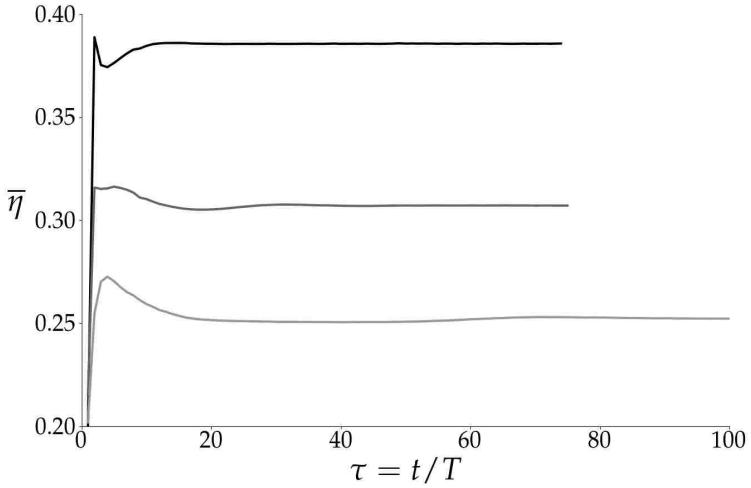

Figure 3.11: Cycle-averaged propulsive efficiency data for a hydrofoil with $k = 1.0$, $D_0^* = 0.25$, and $m^* = 3$ for all St values considered. The line colors, from darkest to lightest, correspond to $St = 0.2, 0.35, 0.5$.

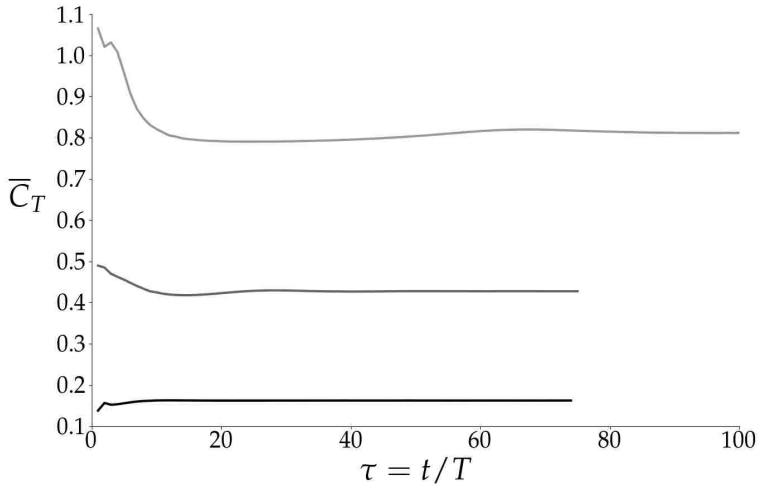

Figure 3.12: Cycle-averaged non-dimensional thrust data for a hydrofoil with $k = 1.0$, $D_0^* = 0.25$, and $m^* = 3$ for all St values considered. The line colors, from darkest to lightest, correspond to $St = 0.2, 0.35, 0.5$.

The wake structures resulting from varying St are presented below in figure 3.13. We observe larger vortex pairs and a more tightly-packed wake structure as a direct result of the increase in pitching amplitude. For the first two St values we see a build up of positive vorticity on the ground plane during steady-state propulsion. As St increases, however, we see this positive vorticity begin to "hover" above the ground plane. It is theorized that propulsors in ground effect with larger St values produce wake structures that induce larger lateral velocities and therefore shift the wake vertically away from the solid boundary.

In an attempt to understand what additional parameters affect an equilibrium position, we present trajectories for equivalent St cases at different k values with $D_0^* = 0.75$, $St = 0.2$, and $m^* = 10$ in figure 3.14:

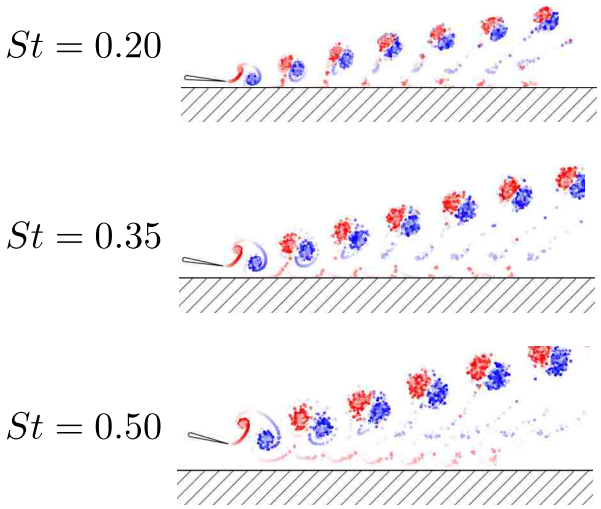

Figure 3.13: Wake structures corresponding to steady-state hydrofoils with $m^* = 3$, $D_0^* = 0.25$, $k = 1.0$ for various St values.

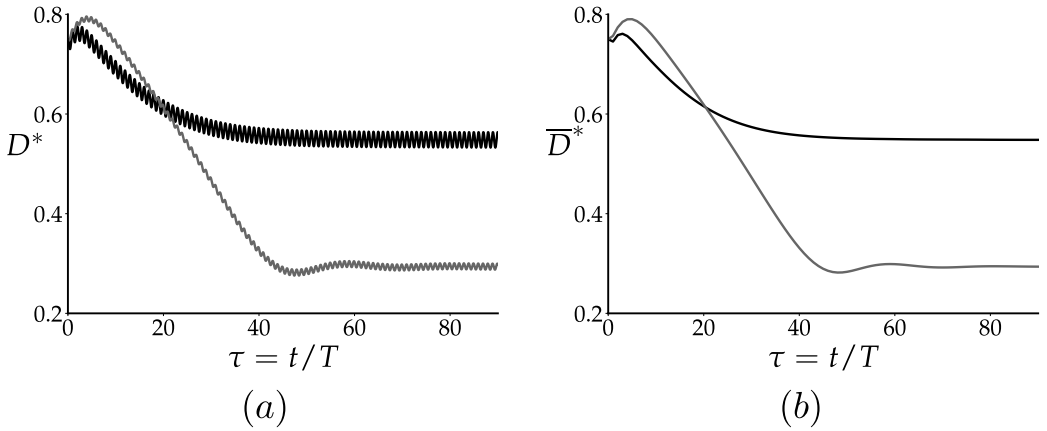

Figure 3.14: Trajectory data for hydrofoils with $D_0^* = 0.75$, $St = 0.2$, and $m^* = 10$ for different k values. (a) Instantaneous leading-edge position. (b) Cycle-averaged leading edge position. The line colors, from darkest to lightest, correspond to $k = 0.5, 1.0$.

Similar to the variations in St, we observe a profound effect on equilibrium position by varying k, so much so that the $k = 2.0$ swimming condition

became unstable. It is clear that St is not the only quantity that alters the location of equilibrium. Larger reduced frequencies appear to manifest as an increase in equilibrium positions. Future endeavors will include scaling relations that attempt to predict equilibrium positions as a function of St, m^*, and k. The performance metrics obtained by varying k are presented in figures 3.15 and 3.16:

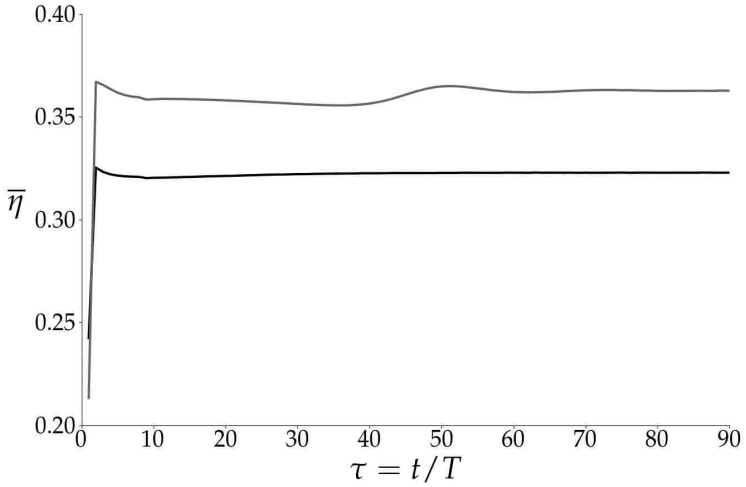

Figure 3.15: Cycle-averaged propulsive efficiency data for a hydrofoil with $D_0^* = 0.75$, $St = 0.2$, and $m^* = 10$ for different k values. The line colors, from darkest to lightest, correspond to $k = 0.5, 1.0$.

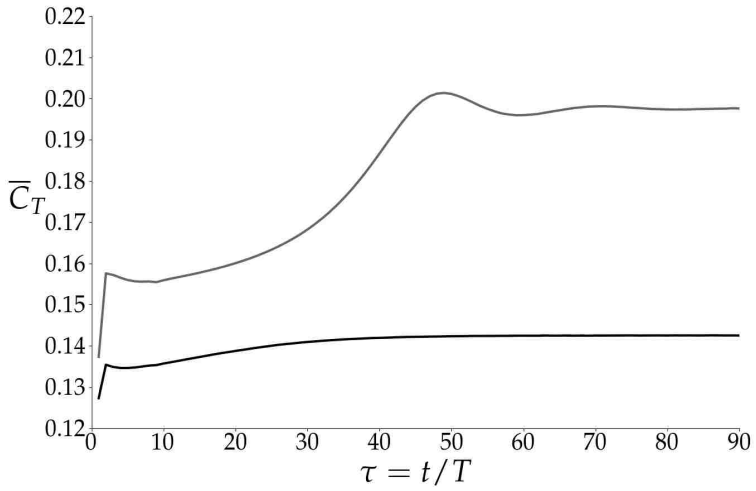

Figure 3.16: Cycle-averaged non-dimensional thrust data for a hydrofoil with $D_0^* = 0.75$, $St = 0.2$, and $m^* = 10$ for all k values considered. The line colors, from darkest to lightest, correspond to $k = \pi/2, \pi$.

We observe larger steady-state thrust values as the frequency of pitching is increased for a constant St value. In addition, it is seen that smaller k values result in larger efficiencies due to smaller pitching amplitudes as a consequence of constant St. The difference in steady-state efficiency, however, is only ~3%. This small disadvantage is met with a ~40% increase in steady-state thrust generation. It is clear that operating at larger pitching frequencies is extremely valuable in unsteady ground effect as the thrust-to-efficiency trade-off favors thrust generation considerably.

The wake structures that correspond to these different k values are presented in figure 3.17 below. We observe smaller vortex pairs in the $k = 1.0$ case as a consequence of the reduction in pitching amplitude for a constant St number. In addition, we see more vortex pairs in the wake for the $k = 1.0$ case due to the increase of pitch cycles per unit time span. Larger pitching

frequencies seem to result in trails of predominantly negative vorticity leading to each vortex pair downstream of the propulsor.

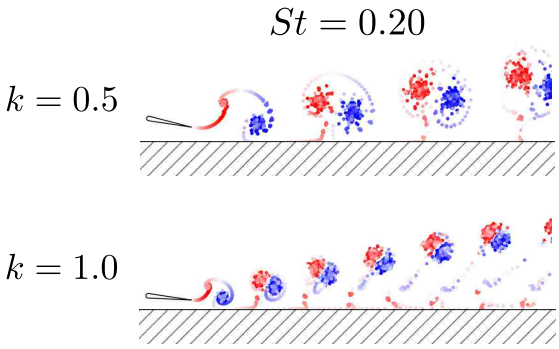

Figure 3.17: Wake structures corresponding to steady-state hydrofoils with $D_0^* = 0.75$, $St = 0.2$, and $m^* = 10$ for various k values.

It has become clear that a number of propulsive benefits may be obtained for hydrofoils in unsteady ground effect. An efficient propolsor will have a small mass and operate at low St and k values. Larger thrust values may result by increasing these quantities at the expense of efficiency. We intend to see how these results change when an additional translational degree-of-freedom is implemented.

3.2 Multiple Translational Degrees of Freedom

We now unlock the propulsor's ability to propel itself in the streamwise direction in accordance with equations (2.73) and (2.75) to observe its effect on performance and wake structure. The performance metrics of interest are now changed to assess the hydrofoil's self-propelling capabilities. We analyze the cycle-averaged swimming speed, $\overline{U}$, in favor of $\overline{C}_{T,net}$. The cycle-averaged propulsive efficiency, $\overline{\eta}$, will also be reported with an altered definition:

$$\overline{\eta} = \frac{\overline{TU}}{\overline{P}} \tag{3.1}$$

It is worth noting that the definition of steady-state changes due to the implementation of a new degree-of-freedom. Steady-state is now achieved when the cycle-averaged lift and net-thrust forces acting on the hydrofoil become sufficiently small ($\overline{C}_L, \overline{C}_{T,net} = \mathcal{O}(10^{-5})$). These conditions result in a propulsor that maintains a constant cycle-averaged lateral position and freestream velocity.

The propulsor's sensitivity to initial pitch direction is analyzed once again for a single simulation presented below in figure 3.18. It can be observed that the solution is insensitive to initial pitch condition. The trajectory exhibits the same trend presented in the single degree-of-freedom case in that the solution differs only during the transient portion of the problem and both initial conditions result in identical equilibrium locations. It appears, however, that the addition of a new degree-of-freedom results in longer convergence times and

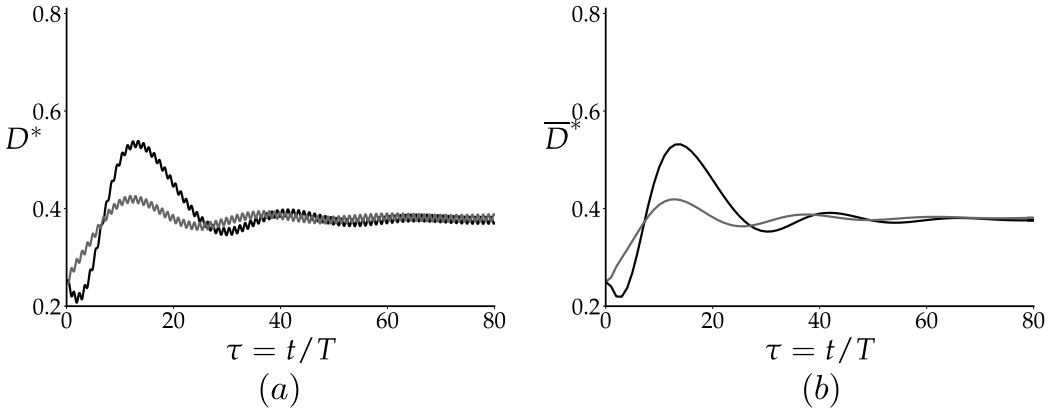

Figure 3.18: Trajectory data for hydrofoils with $D_0^* = 0.25$, $A^* = 0.25$, and $m^* = 10$ for different initial pitch directions. (a) Instantaneous leading-edge position. (b) Cycle-averaged leading edge position. The line colors, from darkest to lightest, correspond to $\phi = 0°, 180°$.

larger overshoots of the equilibrium location. This effect is exacerbated for the pitch up condition where the propulsor initially moves towards the ground where larger lift forces are experienced.

The effect of initial lateral position, D_0^*, is also reassessed in figure 3.19. It appears that the steady-state, cycle-averaged lateral position of the propulsor does not depend on initial position for the multiple degree-of-freedom simulation cases. This finding is consistent with the single degree-of-freedom results seen in figure 3.2. The simulation cases that place the propulsor above the equilibrium plane ($D_0^* = 0.50$, 0.75) exhibit roughly the same amount of equilibrium overshoot, suggesting that ground proximity resulting in extreme ground effect is the primary mechanism behind excessive overshoot.

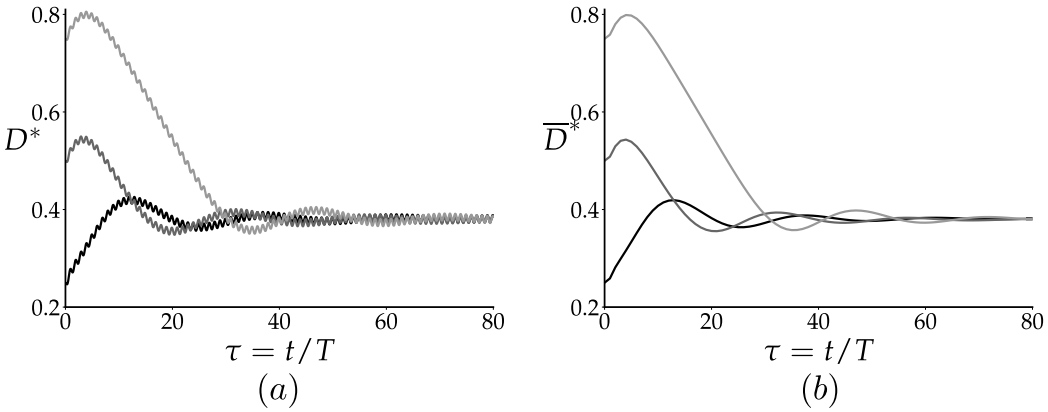

Figure 3.19: Trajectory data for hydrofoils with $A^* = 0.25$ and $m^* = 10$ for all D_0^* values considered. (a) Instantaneous leading-edge position. (b) Cycle-averaged leading edge position. The line colors, from darkest to lightest, correspond to $D_0^* = 0.25, 0.50, 0.75$

The wake structures generated by the hydrofoils for different initial lateral positions are presented in figure 3.20. There appears to be no discernible

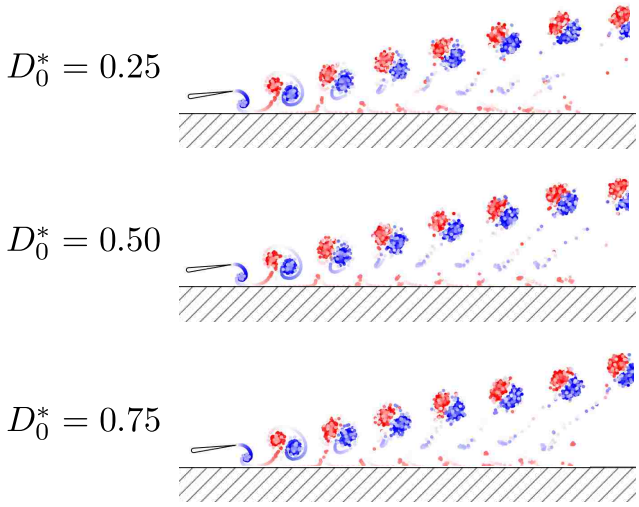

Figure 3.20: Wake structures corresponding to steady-state hydrofoils with $A^* = 0.25$ and $m^* = 10$ for various initial pitching (ϕ) conditions.

differences in wake pattern or vortex trajectory. This finding coincides with the results presented in the single degree-of-freedom case (figure 3.4 and suggests that steady-state wake structures are only dictated by pitching kinematics.

The hydrofoil's trajectory response is now plotted as a function of m^* to discern its effect on equilibrium in figure 3.21:

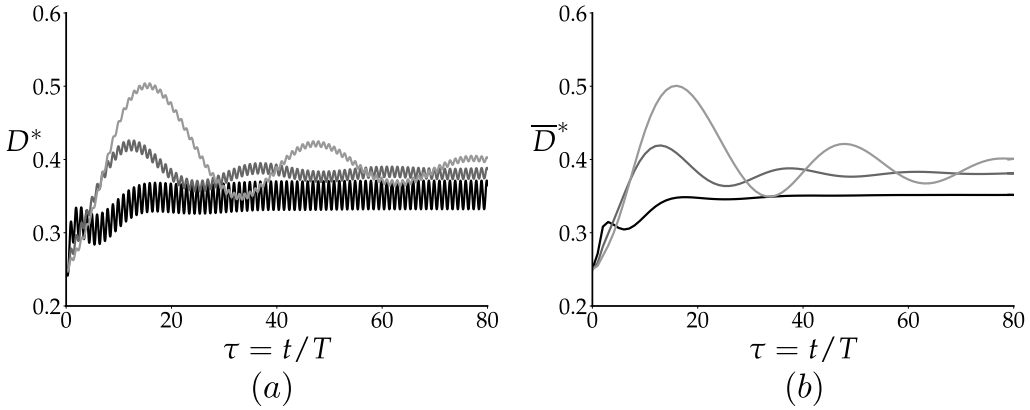

Figure 3.21: Trajectory data for hydrofoils with $A^* = 0.25$ and $D_0^* = 0.25$ for all m^* values considered. (a) Instantaneous leading-edge position. (b) Cycle-averaged leading edge position. The line colors, from darkest to lightest, correspond to $m^* = 3, 10, 20$

We observe that smaller m^* values result in equilibrium positions closer to the solid boundary and larger leading edge oscillations. Again, these finds coincide with those reported in the previous section. However, we observe larger cycle-averaged oscillations at relatively low pitching amplitudes. These findings align more closely with the results for modest pitching amplitudes presented in figure 3.5 for a single degree-of-freedom. It is clear that the additional degree-of-freedom has more profound implications on the hydrofoil's trajectory when considering body mass.

Our analysis now turn towards performance metrics. We present cycle-averaged propulsive efficiency and swimming speed for hydrofoils with varying non-dimensional mass values in figures 3.22 and 3.23, respectively.

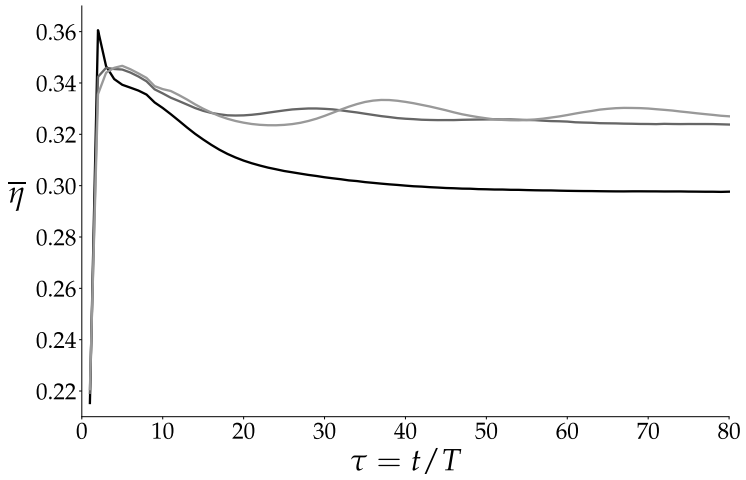

Figure 3.22: Cycle-averaged propulsive efficiency data for a hydrofoil with $A^* = 0.25$ and $D_0^* = 0.25$ for all m^* values considered. The line colors, from darkest to lightest, correspond to $m^* = 3, 10, 20$.

It can be seen that propulsors with smaller masses propel themselves less efficiently near a solid boundary. This finding directly contradicts those reported by figure 3.8 in the previous section. We hypothesize that this role reversal is due to the reduction in steady-state swimming speed for smaller m^* values as seen in figure 3.23. Following equation (3.1), smaller propulsion speeds result in smaller propulsive efficiencies when thrust and power input remain constant. We theorize that a larger portion of the input energy is utilized in the generation of cross-stream kinetic energy than streamwise kinetic energy for low m^* values.

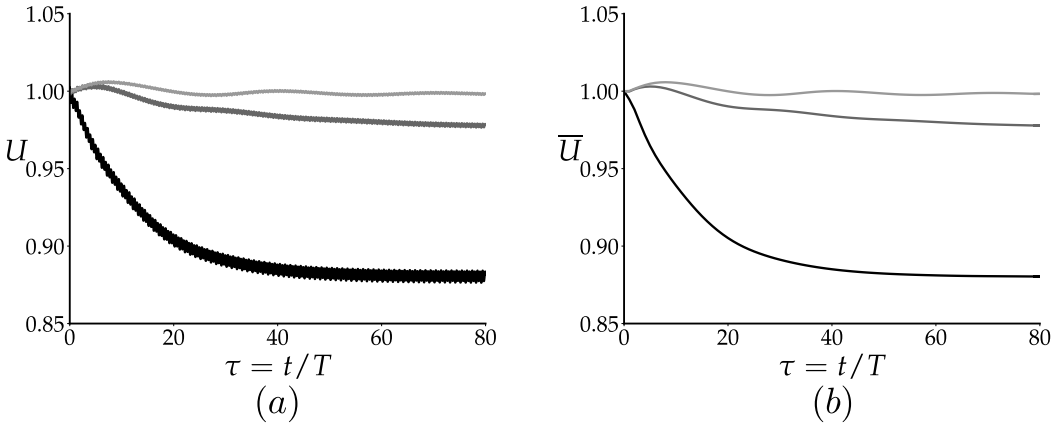

Figure 3.23: Swimming speed data for a hydrofoil with $A^* = 0.25$ and $D_0^* = 0.25$ for all m^* values considered. (a) Instantaneous freestream velocity. (b) Cycle-averaged freestream velocity. The line colors, from darkest to lightest, correspond to $m^* = 3, 10, 20$.

We observe larger fluctuations in the instantaneous streamwise swimming speed for lower m^* values. Similar to the oscillations in the instantaneous trajectory data, smaller m^* values produce larger accelerations and therefore alter instantaneous velocity values accordingly.

The output parameter St is evaluated for each non-dimensional mass case. It appears that the steady-state swimming speed (and therefore St) change by a maximum of ~10% for the range of m^* values considered. We observe a range of St from $0.25 - 0.28$. It appears that smaller non-dimensional mass values correspond to larger steady-state St values for identical pitching kinematics. The m^* value may be finely tuned in future works to result in St values that align more closely with the range evaluated in the previous section for more accurate comparisons.

The wake structures resulting from propulsors with different masses are presented in figure 3.24.

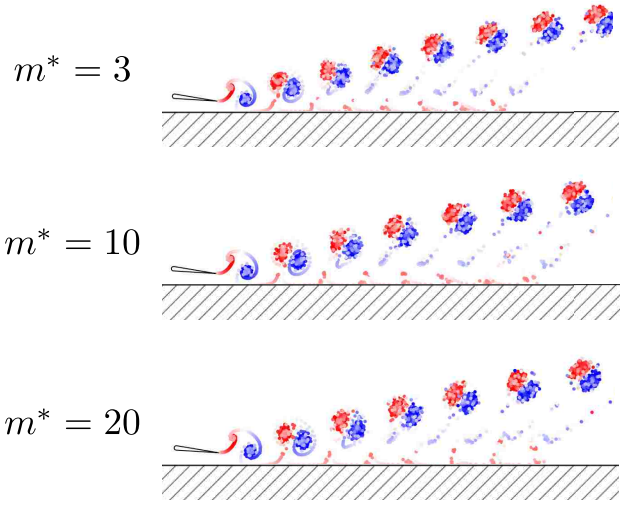

Figure 3.24: Wake structures corresponding to steady-state hydrofoils with $A^* = 0.25$ and $D_0^* = 0.25$ for various m^* values.

We observe negligible changes in the overall vortex pair trajectory angle and vortex pair size for all mass values considered. This conclusion is identical to that drawn in the single degree-of-freedom analysis. It is hypothesized, however, that propulsors with a sufficiently small mass will find equilibrium locations much closer to the wall and therefore produce highly deflected wakes with large vortex pair trajectory angles.

The remainder of the parameter space is probed by varying the non-dimensional peak-to-peak pitching amplitude A^*. The trajectories for propulsors with varying pitching amplitudes is presented below in figure 3.25.

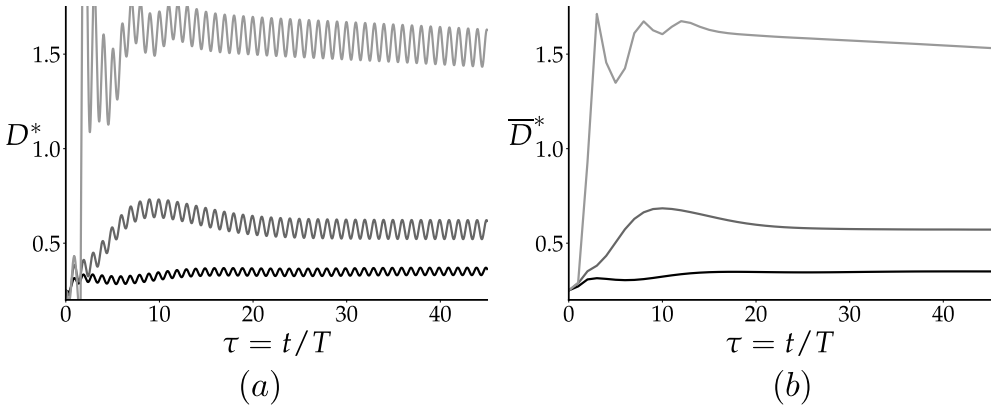

Figure 3.25: Trajectory data for hydrofoils with $D_0^* = 0.25$ and $m^* = 3$ for all A^* values considered. (a) Instantaneous leading-edge position. (b) Cycle-averaged leading edge position. The line colors, from darkest to lightest, correspond to $A^* = 0.25, 0.5, 0.75$.

An increase in pitching amplitude appears to shift the equilibrium position away from the solid boundary, increase convergence time, and increase leading edge oscillations. The $A^* = 0.25, 0.5$ cases remained stable and found a distinct steady-state lateral position after approximately 20 and 30 pitching cycles, respectively. However the largest A^* value grew unstable after 1 pitching cycle as a result of extreme ground proximity. The hydrofoil is able to recover, however, and exhibits a more predictable trajectory. The following analysis will only consider the latter hydrofoil's physical, steady-state performance results due to initial instabilities.

The cycle-averaged propulsive efficiency and swimming speed for hydrofoils with varying non-dimensional pitching amplitudes is presented in figures 3.26 and 3.27, respectively.

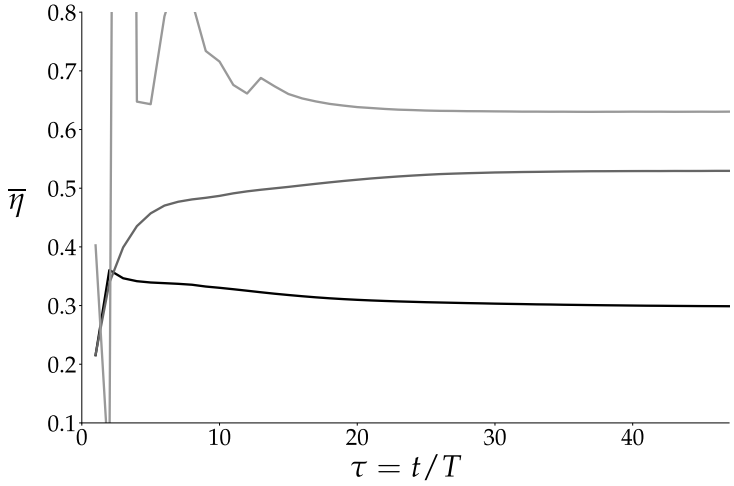

Figure 3.26: Cycle-averaged propulsive efficiency data for a hydrofoil with $D_0^* = 0.25$ and $m^* = 3$ for all A^* values considered. The line colors, from darkest to lightest, correspond to $A^* = 0.25, 0.5, 0.75$.

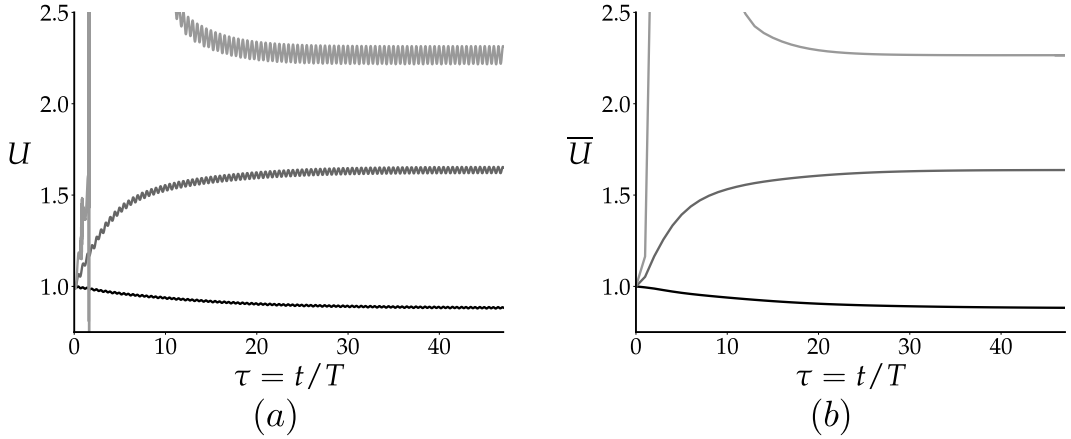

Figure 3.27: Swimming speed data for a hydrofoil with $D_0^* = 0.25$ and $m^* = 3$ for all A^* values considered. (a) Instantaneous freestream velocity. (b) Cycle-averaged freestream velocity. The line colors, from darkest to lightest, correspond to $A^* = 0.25, 0.5, 0.75$.

It appears that larger pitching amplitudes correspond to larger propulsive efficiencies. We observe a smaller steady-state efficiency increase as we linearly increase the pitching angle, suggesting there is a theoretical maximum propulsive efficiency that may be achieved. This conclusion appears to go against those reported in figure 3.11. Although this finding may be attributed to the presence of a solid-boundary, it may be non-physical and unrealistic for the present Li number and pitching kinematics.

In addition, we observe larger cycled-averaged steady-state swimming speeds and instantaneous swimming speed fluctuations as pitching angle increases. There is a clear transition from an initially decelerating swimming regime to an initially accelerating swimming regime between $A^* = 0.25$ and $A^* = 0.50$. The steady-state St results for the variation in pitching amplitude correspond to $St = 0.28, 0.30, 0.33$ for increasing A^*. The effect of pitching amplitude on multiple degree-of-freedom propulsion conditions will be probed further in future works to investigate these rather counter-intuitive findings.

The wake structures corresponding to a variation in non-dimensional pitch amplitude are now presented below in figure 3.28. The first two pitching amplitudes considered, $A^* = 0.25, 0.50$, possess wake structures that interact with the solid boundary to form familiar vortex pairs. The $A^* = 0.75$ case, however, gravitates toward an equilibrium position sufficiently far from the ground where its wake remains largely unaffected undisturbed by the solid boundary. We see a traditional 2S reverse von Kármán street that is typically produced in isolated swimming. There appears to be a critical equilibrium plane where the presence of the wall no longer affects wake structure development. The

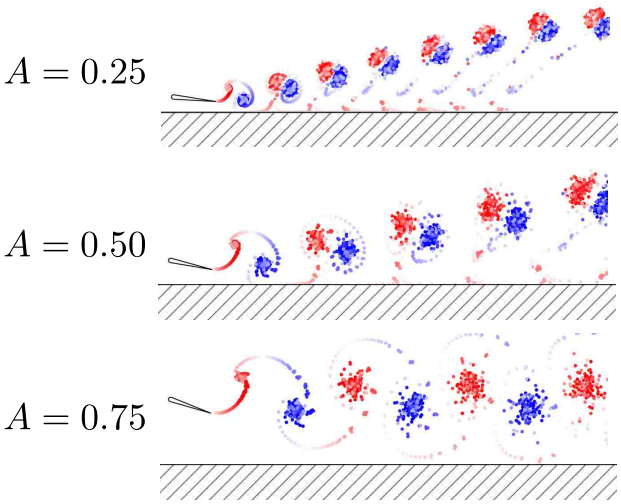

Figure 3.28: Wake structures corresponding to steady-state hydrofoils with $D_0^* = 0.25$ and $m^* = 3$ for various A^* values.

parameters that affect the position of this critical plane and the propulsor's performance at this spacial location will be investigated further by utilizing more granular parameter spaces in the near future.

Chapter 4

Conclusion

This thesis presents a computational method for the study of bio-inspired propulsors in unsteady ground effect. An unsteady potential flow model is coupled with a free-swimming dynamics model to calculate hydrodynamic loading, propulsive efficiency, and trajectory data for self-propelled pitching hydrofoils in moderate to extreme ground effect.

Two distinct parameter spaces are probed to discern the effect of kinematic and physical variables on self-propulsion in single and multiple translational degree-of-freedom swimming conditions. It is found that stable equilibrium positions exist at a distance away from the solid boundary where the cycle-averaged lift forces approach zero for both degree-of-freedom cases. The exact location of this equilibrium position appears to be governed by pitch amplitude, pitch frequency, and non-dimensional mass.

The hydrodynamic performance of the ground effect propulsor was found to exceed that of its isolated counterpart in propulsive efficiency and/or thrust

generation for single degree-of-freedom conditions. The multiple degree-of-freedom cases uncovered different magnitudes of thrust-producing regimes contingent upon pitching amplitude and non-dimensional mass. An increase in pitching amplitude resulted in increases in both propulsive efficiency and swimming speed due to the presence of the solid boundary.

4.1 Future Work

The scope of the parameter space will be expanded upon in order to learn more about the implications of unsteady ground effect. Additional C_D and S_{wp} values may be explored in an attempt to mirror the physical characteristics exhibited by currently identified ground swimmers to draw more concrete conclusions with biologically relevant data. The parameters corresponding to kinematic behavior will also be studied more granularly in an attempt to uncover more subtle phenomena resulting from unsteady ground effect. Rotational degrees-of-freedom are then to be implemented for a more accurate representation of a self-propelled swimmer.

The results presented in this thesis will be compared against experimental unsteady ground effect data to discern if the benefits discovered are a consequence of the assumptions of the model.

Bibliography

[1] I. Dobrev F. Massouh V Cognet, S. Courrech du Pont and B. Thiria. Bioinspired turbine blades offer new perspectives for wind energy. 473(2198), 2017.

[2] Justin W. Jaworski and N. Peake. Aerodynamic noise from a poroelastic edge with implications for the silent flight of owls. *Journal of Fluid Mechanics*, 723:456–479, 2013.

[3] George V. Lauder. Fish locomotion: Recent advances and new directions. *Annual Review of Marine Science*, 7(1):521–545, 2015.

[4] P. W. Webb. The swimming energetics of trout. *Journal of Experimental Biology*, 55(2):521–540, 1971.

[5] T. L. Williams J. Carling and G. Bowtell. Self-propelled anguilliform swimming: simultaneous solution of the two-dimensional navier-stokes equations and newton's laws of motion. *Journal of Experimental Biology*, 201(23):3143–3166, 1998.

[6] Iman Borazjaniand and Fotis Sotiropoulos. Numerical investigation of the hydrodynamics of carangiform swimming in the transitional and inertial flow regimes. *Journal of Experimental Biology*, 211(10):1541–1558, 2008.

[7] Knut Schmidt-Nielsen. Locomotion: Energy cost of swimming, flying, and running. *Science*, 177(4045):222–228, 1972.

[8] C. Coulliette and A. Plotkin. Airfoil ground effect revisited. *Aeronautical Journal*, 100:65–74, 1996.

[9] R. V. Baudinette and K. Schmidt-Nielsen. Energy cost of gliding flight in herring gulls. *Nature*, 248:83–84, 1974.

[10] Benjamin Thiria Francisco Huera-Huarte Rafael Fernández-Prats, Veronica Raspa and Ramiro Godoy-Diana. Large-amplitude undulatory swimming near a wall. *Bioinspiration and Biomimetics*, 10:016003, 2015.

[11] Thomas Engels Hao Liu Kai Schneider Dmitry Kolomenskiy, Masateru Maeda and Jean-Christophe Nave. Aerodynamic ground effect in fruitfly sized insect takeoff. *PLOS ONE*, 11:1–21, 2016.

[12] W. P. Webb. The effect of solid and porous channel walls on steady swimming of steelhead trout, oncorhynchus mykiss. *J. Expl. Biol.*, 178:97–108, 1993.

[13] Gil Iosilevskii. Asymptotic theory of an oscillating wing section in weak ground effect. *European Journal of Mechanics - B/Fluids*, 27(4):477 – 490, 2008.

[14] Yoshimichi Tanida. Ground effect in flight. 44:481–486, 2001.

[15] Mao Sun and Jian Tang. Unsteady aerodynamic force generation by a model fruit fly wing in flapping motion. *Journal of Experimental Biology*, 205(1):55–70, 2002.

[16] J. Wu and N. Zhao. Ground effect on flapping wing. *Procedia Engineering*, 67:295 – 302, 2013.

[17] Yair Moryossef and Yuval Levy. Effect of oscillations on airfoils in close proximity to the ground. *AIAA Journal*, 42:1755–1764, 2004.

[18] Juan Molina and Xin Zhang. Aerodynamics of a heaving airfoil in ground effect. *AIAA Journal*, 49:1168–1179, 2011.

[19] George V. Lauder Daniel B. Quinn and Alexander J. Smits. Flexible propulsors in ground effect. *Bioinspiration and Biomimetics*, 9(3):036008, 2014.

[20] Erin Blevins and George Lauder. Swimming near the substrate: A simple robotic model of stingray locomotion. *Bioinspiration and biomimetics*, 8:016005, 2013.

[21] P. A Dewey D. B Quinn, K. W. Moored and A. J Smits. Unsteady propulsion near a solid boundary. *Journal of Fluid Mechanics*, 742:152–170, 2014.

[22] D. Young B. Munson and T. Okiishi. *Fundamentals of fluid mechanics.* Wiley, New York, NY:, 1998.

[23] Wade R. Mcgillis Erik J. Anderson and Mark A. Grosenbaugh. The boundary layer of swimming fish. *Journal of Experimental Biology*, 204:81–102, 2001.

[24] P. T. Kostecki P. W. Webb and E. Don Stevens. The effect of size and swimming speed on locomotor kinematics of rainbow trout. *Journal of Experimental Biology*, 109:77–95, 1984.

[25] D Weihs JJ Videler. Energetic advantages of burst-and-coast swimming of fish at high speeds. *Journal of Experimental Biology*, 97:169–178, 1982.

[26] JJ Videler. Swimming movements, body structure and propulsion in cod gadus morhua. *Symp. Zool. Soc. Lond*, 48:1–27, 1981.

[27] Yan Yang Guanhao Wu and Lijiang Zeng. Kinematics, hydrodynamics and energetic advantages of burst-and-coast swimming of koi carps (cyprinus carpio koi). *Journal of Experimental Biology*, 210:2181–2191, 2007.

[28] Uwe Ehrenstein and Christophe Eloy. Skin friction on a moving wall and its implications for swimming animals. *Journal of Fluid Mechanics*, 718:321–346, 2013.

[29] Matthieu Marquillie Uwe Ehrenstein and Christophe Eloy. Skin friction on a flapping plate in uniform flow. *Phil. Trans. R. Soc. A*, 372:20130345, 2014.

[30] Keith W Moored and Daniel B Quinn. Inviscid scaling laws of a self-propelled pitching airfoil. 2017. Preprint arXiv:1703.08225.

[31] Christophe Eloy. Optimal strouhal number for swimming animals. *Journal of Fluids and Structures*, 30:205–218, 2012.

[32] Jean-Luc Aider Ramiro Godoy-Diana, Catherine Marais and José Eduardo Wesfreid. A model for the symmetry breaking of the reverse bénard–von kármán vortex street produced by a flapping foil. *Journal of Fluid Mechanics*, 622:23–32, 2009.

[33] E. Akoz and K. W. Moored. Unsteady propulsion by an intermittent swimming gait. *Journal of Fluid Mechanics*, 834:149–172, 2018.

[34] J. Katz and A. Plotkin. *Low-speed aerodynamics*. Cambridge University Press, New York, NY, second edition, 2001.

[35] J. Peraire D. J. Willis and J. K. White. A combined pfft-multipole tree code, unsteady panel method with vortex particle wakes. *Intl J. Numer. Meth. Fluids*, 53:1399–1422.

[36] Robert Krasny. A study of singularity formation in a vortex sheet by the point-vortex approximation. *Journal of Fluid Mechanics*, 167:65–93, 1986.

[37] K. W. Moored. Unsteady three-dimensional boundary element method for self-propelled bio-inspired locomotion. *Computers and Fluids*, 167:324–340, 2017.

[38] T. Theodorsen. General theory of aerodynamic instability and the mechanism of flutter. *NACA Tech. Rep*, 496, 1935.

[39] I. E. Garrick. Propulsion of a flapping and oscillating airfoil. *NACA Tech. Rep*, 567, 1936.

[40] L. Ge I. Borazjani and F. Sotiropoulos. Curvilinear immersed boundary method for simulating fluid structure interaction with complex 3d rigid bodies. *Journal of Computational Physics*, 227:7587–7620, 2008.

Vita

Jackson Heath Cochran-Carney was born in Marshfield, Wisconsin on November 18th, 1994 to Jeffrey Carney and Cynthia Cochran. He graduated *summa cum laude* from Lehigh University in 2017 with a Bachelors of Science in Mechanical Engineering and a minor in Aerospace Engineering. He began work on his Master's of Science in Mechanical Engineering as a Presidential Scholar at Lehigh University later that same year under Dr. Keith Moored within the Bio-Fluids Laboratory.